# INTERPLAY BETWEEN SINGLE-PARTICLE AND COLLECTIVE MOTION WITHIN NUCLEAR DENSITY FUNCTIONAL THEORY

By

Chunli Zhang

A DISSERTATION

Submitted to
Michigan State University
in partial fulfillment of the requirements
for the degree of

Physics — Doctor of Philosophy

2016

## ABSTRACT

## INTERPLAY BETWEEN SINGLE-PARTICLE AND COLLECTIVE MOTION WITHIN NUCLEAR DENSITY FUNCTIONAL THEORY

**By**

**Chunli Zhang**

Nuclear density functional theory (DFT) can be employed to study properties of ground states (g.s.) and selected excited states of nuclei anywhere in the nuclear chart. The focus of this work is on the description of single-particle (s.p.) and collective motion in nuclei using nuclear DFT. Since nuclear collective phenomena result from a coherent motion of individual nucleons, the sharp distinction between these two modes cannot be made. For example, nuclear rotation leads to the alignment of angular momentum with rotational frequency, which results in the variation of occupations in s.p. orbitals. Spontaneous fission leads to not only large geometrical rearrangements, but also impacts the internal shell structure.

This dissertation is divided into three parts. In the first part, I shall briefly introduce the nuclear model used. In the second part, the general formalism of nuclear DFT and its main ingredient, the energy density functional (EDF) will be outlined. In the last part, the applications of nuclear DFT will be presented. First, we study the nuclear shapes and associated rotational bands for nuclei with $A \approx 110$; yrast, near-yrast band structures, angular momentum alignments with rotational frequency, and transition quadrupole moments are analyzed and compared to experimental data. Then, based on the Kerman-Onishi condition, we perform systematic tilted-axis-cranking calculations for triaxial strongly deformed (TSD) bands in $^{160}$Yb, explain the nature of these TSD bands, and predict possible collective behavior at high spin. Next we explore cluster structures in light nuclei using the novel concept of the nucleon localization function (NLF). The NLF is then used to study the internal structure

evolution and emergence of fragments in fissioning heavy nuclei along their predicted fission pathways. We then show that the NLF can be employed to identify fission fragments well before scission in $^{240}$Pu. The last section contains the conclusions of this dissertation and offers perspectives for future work.

*This dissertation is dedicated to my grandparents.*

## ACKNOWLEDGMENTS

First of all, I would like to thank my advisor, Prof. Witold Nazarewicz, for his outstanding guidance and insightful advice. The attitude toward scientific research which I learned from him will be of endless benefit to my life.

I would like to express my gratitude to all my colleagues for their advice and help with both research and life, especially Yue Shi, Bastian Schuetrumpf, Erik Olsen, Yannen Jaganathen, Kevin Fossez and Simin Wang.

I would like to thank Nobuo Hinohara, Jhilam Sadhukhan and Nicolas Schunck for their generous help with my research and endless patience with all my questions.

The work presented in this dissertation was carried out at The University of Tennessee, Knoxville (UTK) from 2012 to 2014 and Michigan State University (MSU) from 2014 to 2016. I would like to thank the staff members at UTK and MSU for their help.

I would like to thank Zachary Matteson and Erik Olsen for reading and help with editing my dissertation.

I would like to thank Filomena Nunes, Scott Bogner, Alexandra Gade, and Carlo Piermarocchi for serving on my doctoral committee.

I am very grateful to my parents for their unconditional love and support.

I am very grateful to my husband, Zhiling Dun, for his company and encouragement.

# TABLE OF CONTENTS

# LIST OF TABLES

# LIST OF FIGURES

# Chapter 1

# Introduction

The atomic nucleus is a strongly-correlated, self-bound many-body system, which exhibits a variety of collective and single-particle non-collective phenomena. In collective motion, many nucleons are involved, for example, nuclear vibration, nuclear rotation, fission, which could result in external observable property changes. While in single-particle motion individual nucleons move independently, internal structures governed by shell effects are impacted, which can cause the particle-hole excitation, pair breaking and clustering of nucleons. Numerous microscopic theoretical approaches have been developed to study nuclear structure. They can be grouped into three general categories: *ab initio* methods [9–13], shell model (or configuration interaction) theories [14, 15] and nuclear DFT based on the self-consistent mean field approach [16, 17].

In this dissertation, the main topic of study is collective motion, including (i) nuclear rotation based on triaxial configurations that exhibit strong quadrupole collectivity and (ii) spontaneous fission in heavy nuclei that is associated with quadrupole and octupole collective dynamics through large-amplitude collective motion. Since nuclear DFT describes nuclear systems in terms of local densities, the resulting spontaneous symmetry breaking effects [18, 19] can be employed to define nuclear geometries.

On the other hand, there is always a subtle interplay between collective and s.p. motion at the same energy scale. For example, as the rotational frequency increases, the alignment of angular momentum within the collective rotational band can lead to band-crossing [18,20,21],

at which the lowest (yrast) configuration will change rapidly. In self-consistent mean-field methods based on nuclear DFT, the change of s.p. configurations can be expressed through occupations of s.p. orbitals. The resulting structural changes can be described using the cranking approach, where the nuclear motion is described in the rotating reference frame. By the same token, in spontaneous fission, as the system evolves along the fission pathway, its internal shell structure is impacted dramatically. Here, our strategy is to introduce the nucleon localization function [22], which will help to visualize nucleon clustering and correlations imprinted by shell effects.

The dissertation is organized as follows. Nuclear DFT is introduced in Chap. 2. Applications to triaxial structures are explored in Chap. 3. In Chap. 4, the nucleon localization function [23,24] is employed to illustrate the emergence of clustering structures in light nuclei and fission fragments in heavy nuclei. Finally, conclusions and prospects for future work are summarized in Chap. 5. A brief introduction to these chapters is given in the following.

## 1.1 Nuclear density functional theory

Since the nucleus is a self-bound system which may display both individual nucleon excitations and collective excitations at the same energy scale, it is a challenge to describe it using a single theoretical framework. Nuclear DFT incorporates nucleon correlations by introducing complex density dependence into EDFs, while collective motion can be considered explicitly by introducing Lagrange multipliers to constrain the collective coordinates, such as nuclear multipole moments and angular momentum. Nuclear DFT is a flexible tool; it has been employed to a variety of phenomena, including shape deformations [17, 25], neutron/proton drip-lines [26], two-proton decay [27], (large-amplitude) collective motion [17, 28, 29], and

nuclear pasta [30, 31] in neutron stars. Since the scope of our research ranges from light to heavy nuclei, nuclear DFT is our tool of choice.

## 1.2 Nuclear shapes and collective motion

The atomic nucleus can exhibit different shapes, for example, spherical, prolate/oblate, triaxial, pear-like, etc. The collective rotation of a spherical nucleus is impossible due to the indistinguishability of rotated configurations, while a deformed nucleus can exhibit collective rotational motion that results in the presence of rotational bands [18, 32]. The most common case of this is an axially deformed nucleus with prolate or oblate shape, with angular momentum built along the axis that is perpendicular to the symmetry axis of the system. Another less common case is that of the triaxial nucleus. Here, the collective angular momentum can be aligned in any direction as the axial symmetry of the system is broken. Experiment provides very indirect information about triaxial configurations. Theoretically, very few nuclei are predicted to be triaxially deformed in their ground states.

Theoretically, the macroscopic-microscopic model [33] and traditional cranked shell model [34, 35] have been employed to study nuclear shapes and rotations. However, unlike relativistic [6, 36] and non-relativistic [37, 38] mean-field models, those approaches are not self-consistent, and this constitutes a major problem. In my research, nuclear DFT with recently optimized EDFs is applied to study triaxial shapes and rotational motion in the $A \approx 110$ region and high-spin bands in $^{160}$Yb interpreted in terms of TSD structures. By solving the cranked Hartree-Fock and Hartree-Fock-Bogoliubov equations, characteristic features of rotational bands, such as band-crossings and shape changes, will be studied.

## 1.3 Nucleonic clustering

The appearance of cluster states in atomic nuclei is a ubiquitous phenomenon with many implications for both nuclear physics and astrophysics [39–43]. While several factors are known to contribute to clustering, a comprehensive microscopic understanding of this phenomenon still remains elusive. Cluster configurations can be energetically favored due to the large binding energy per nucleon in constituent clusters, such as $\alpha$ particles. This binding-energy argument has often been used to explain properties of $\alpha$-conjugate nuclei [44], cluster emission [45, 46] and fission [47], and the appearance of a gas of light clusters in low-density nuclear matter [48–50] and in the interior region of heavy nuclei [51]. Another important factor is the coupling of cluster states to decay channels, which explains [52, 53] their occurrence at low excitation energies around cluster-decay thresholds [54].

The microscopic description of cluster states requires the use of an advanced many-body, open-system framework [52, 53, 55] employing realistic interactions, and there has been significant progress in this area [56–60]. Theoretically, the Bloch-Brink alpha-cluster and antisymmetrized molecular dynamics models [39–41] have been used to describe cluster states. The former adopts multi-center cluster wave functions and is parametrized by the geometry of cluster center positions; it is mainly used in $\alpha$-conjugate nuclei assuming the existence of cluster states. The latter is based on a Slater determinant consisting of Gaussian wave packets.

For a global characterization of cluster states in light and heavy nuclei, a good starting point is nuclear DFT. Here, cluster states have a simple interpretation in terms of quasi-molecular structures. Since the mean-field approach is rooted in the variational principle, the binding-energy argument favors clustering in certain configurations characterized by large

shell effects of constituent fragments [61–68]; the characteristics of cluster states can be indeed traced back to the symmetries and geometry of the nuclear mean-field [69, 70].

# Chapter 2

# Theoretical Tool: Nuclear DFT

In this chapter, the theoretical model used in my research is described. In section 2.1, we shall outline the theoretical foundations of nuclear DFT; the single-reference Skyrme EDF used in this work is introduced in section 2.2. In section 2.3, the self-consistent Skyrme EDF method is presented, and I explain how the mean-field equations can be solved. Finally, the nuclear DFT solvers used in my research, and their characteristics and limitations, are discussed in section 2.4.

## 2.1 General consideration and formalism

The Hamiltonian of a many-body system can be written as:

$$\hat{H} = \hat{T} + \hat{V} + \hat{U}_{\text{ext}}, \tag{2.1}$$

where $V$ is the inter-particle interaction and $U_{\text{ext}}$ is the external field. The eigenstates of the interacting system $|\Psi\rangle$ can be obtained by, e.g., diagonalizing the Hamiltonian, and the one-body local nucleonic density can be written as:

$$\rho(\boldsymbol{r}) = N \int d\boldsymbol{r}_2 \cdots d\boldsymbol{r}_A |\Psi(\boldsymbol{r}, \boldsymbol{r}_2, \cdots, \boldsymbol{r}_A)|^2. \tag{2.2}$$

DFT is rooted in the theorems formulated by Hohenberg and Kohn [71]. It was originally

used to investigate electronic structure in quantum chemistry and condensed matter physics, and - in parallel developments - was extended to nuclear physics as well. Hohenberg and Kohn demonstrated [71] that there exists a universal functional of the density, $F[\rho(\boldsymbol{r})]$, independent of external potential, $U_{\text{ext}}$, such that the total energy, $E \equiv F[\rho(\boldsymbol{r})] + \int U_{\text{ext}}(\boldsymbol{r})\rho(\boldsymbol{r})d\boldsymbol{r}$, has its minimum at the exact g.s. associated with the external potential (see Appendix A for the demonstration).

Therefore, everything would be simple as long as we knew the universal functional. Hypothetically, one could scan various external potentials and find the functional $E[\rho(\boldsymbol{r})]$ with respect to the density $\rho(\boldsymbol{r})$. However, such a procedure is impossible as we do not know the exact inter-nucleon interaction in medium. There exist various approximation schemes to construct the functional for the energy, e.g., the Skyrme EDF, the Gogny EDF, EDF from effective field theory (EFT), etc. They are derived from the zero-range Skyrme force [72,73], the finite-range Gogny force [74–76] and using the EFT framework [77], respectively, even though $E[\rho]$ in DFT does not have to be associated with any nuclear interaction. In my work, the Skyrme EDF is the functional of choice, primarily due to its simplicity and success in explaining the data; it will be introduced in the next section.

## 2.2 Skyrme energy density functional

For the zero-range Skyrme force, the total energy of the nucleus, as a functional of one-body density and pairing matrices, is given by [78]

$$E[\rho, \tilde{\rho}] = \int \mathcal{H}(\boldsymbol{r})d\boldsymbol{r}, \tag{2.3}$$

where $\mathcal{H}(\boldsymbol{r})$ is a real, scalar, isoscalar, time-even functional of local densities and their derivatives. The Skyrme EDF (2.3) can be decomposed into the kinetic energy density, interaction energy density, pairing energy density, Coulomb energy density, and additional corrections, such as the center-of-mass correction [78]:

$$\mathcal{H}(\boldsymbol{r}) = \mathcal{H}_{\rm Kin}(\boldsymbol{r}) + \mathcal{H}_{\rm Int}(\boldsymbol{r}) + \mathcal{H}_{\rm pairing}(\boldsymbol{r}) + \mathcal{H}_{\rm Coul}(\boldsymbol{r}) + \mathcal{H}_{\rm cor}(\boldsymbol{r}). \tag{2.4}$$

Before we present the form of each term in Eq. (2.4), we shall introduce the local densities used.

### 2.2.1 Local densities

In the mean-field approximation, the one-body nonlocal density and pairing density are defined as

$$\rho_\alpha(\boldsymbol{r}s, \boldsymbol{r}'s') = \langle\Psi|a^\dagger_{\boldsymbol{r}'s'}a_{\boldsymbol{r}s}|\Psi\rangle\,, \tag{2.5a}$$

$$\tilde{\rho}_\alpha(\boldsymbol{r}s, \boldsymbol{r}'s') = -2s'\,\langle\Psi|a_{\boldsymbol{r}'-s'}a_{\boldsymbol{r}s}|\Psi\rangle\,, \tag{2.5b}$$

respectively, where $a^\dagger_{rs}$ and $a_{rs}$ create and annihilate a neutron ($\alpha = n$) or proton ($\alpha = p$) at the space point $\boldsymbol{r}$ with spin $s$, and $|\Psi\rangle$ is a many-body wave function. By expanding the nonlocal particle density and pairing density in spin space, one obtains:

$$\rho_\alpha(\boldsymbol{r}s, \boldsymbol{r}'s') = \frac{1}{2}\rho_\alpha(\boldsymbol{r}, \boldsymbol{r}')\delta_{ss'} + \frac{1}{2}\boldsymbol{s}_\alpha(\boldsymbol{r}, \boldsymbol{r}')\cdot\boldsymbol{\sigma}_{ss'}, \tag{2.6a}$$

$$\tilde{\rho}_\alpha(\boldsymbol{r}s, \boldsymbol{r}'s') = \frac{1}{2}\tilde{\rho}_\alpha(\boldsymbol{r}, \boldsymbol{r}')\delta_{ss'} + \frac{1}{2}\tilde{\boldsymbol{s}}_\alpha(\boldsymbol{r}, \boldsymbol{r}')\cdot\boldsymbol{\sigma}_{ss'}, \tag{2.6b}$$

where $\boldsymbol{\sigma}_{ss'} = (\boldsymbol{\sigma}^x_{ss'}, \boldsymbol{\sigma}^y_{ss'}, \boldsymbol{\sigma}^z_{ss'})$ are spin Pauli matrices and $\rho_\alpha(\boldsymbol{r}, \boldsymbol{r'})$, $\boldsymbol{s}_\alpha(\boldsymbol{r}, \boldsymbol{r'})$, $\tilde{\rho}_\alpha(\boldsymbol{r}, \boldsymbol{r'})$ and $\tilde{\boldsymbol{s}}_\alpha(\boldsymbol{r}, \boldsymbol{r'})$ are derived as

$$\begin{aligned}
\rho_\alpha(\boldsymbol{r}, \boldsymbol{r'}) &= \sum_s \rho_\alpha(\boldsymbol{r}s, \boldsymbol{r'}s), && \text{(2.7a)} \\
\boldsymbol{s}_\alpha(\boldsymbol{r}, \boldsymbol{r'}) &= \sum_{ss'} \rho_\alpha(\boldsymbol{r}s, \boldsymbol{r'}s')\boldsymbol{\sigma}_{ss'}, && \text{(2.7b)} \\
\tilde{\rho}_\alpha(\boldsymbol{r}, \boldsymbol{r'}) &= \sum_s \tilde{\rho}_\alpha(\boldsymbol{r}s, \boldsymbol{r'}s), && \text{(2.7c)} \\
\tilde{\boldsymbol{s}}_\alpha(\boldsymbol{r}, \boldsymbol{r'}) &= \sum_{ss'} \tilde{\rho}_\alpha(\boldsymbol{r}s, \boldsymbol{r'}s')\boldsymbol{\sigma}_{ss'}. && \text{(2.7d)}
\end{aligned}$$

Since the Skyrme EDF is expressed as a functional of local densities and their derivatives, the following nucleonic densities need to be considered [79, 80]:

1. Particle-density $\rho_\alpha(\boldsymbol{r})$ and spin density $\boldsymbol{s}_\alpha(\boldsymbol{r})$:

$$\begin{aligned}
\rho_\alpha(\boldsymbol{r}) &= \rho_\alpha(\boldsymbol{r}, \boldsymbol{r}), && \text{(2.8a)} \\
\boldsymbol{s}_\alpha(\boldsymbol{r}) &= \boldsymbol{s}_\alpha(\boldsymbol{r}, \boldsymbol{r}). && \text{(2.8b)}
\end{aligned}$$

2. Kinetic density $\tau_\alpha(\boldsymbol{r})$ and vector kinetic density $\boldsymbol{T}_\alpha(\boldsymbol{r})$:

$$\begin{aligned}
\tau_\alpha(\boldsymbol{r}) &= [\boldsymbol{\nabla} \cdot \boldsymbol{\nabla'} \rho_\alpha(\boldsymbol{r}, \boldsymbol{r'})]_{\boldsymbol{r}=\boldsymbol{r'}}, && \text{(2.9a)} \\
\boldsymbol{T}_\alpha(\boldsymbol{r}) &= [\boldsymbol{\nabla} \cdot \boldsymbol{\nabla'} \boldsymbol{s}_\alpha(\boldsymbol{r}, \boldsymbol{r'})]_{\boldsymbol{r}=\boldsymbol{r'}}. && \text{(2.9b)}
\end{aligned}$$

3. Momentum density $\boldsymbol{j}_\alpha(\boldsymbol{r})$ and spin-current tensor $\overleftrightarrow{J}_\alpha(\boldsymbol{r})$:

$$\boldsymbol{j}_\alpha(\boldsymbol{r}) = \frac{1}{2i}[(\boldsymbol{\nabla} - \boldsymbol{\nabla'})\rho_\alpha(\boldsymbol{r}, \boldsymbol{r'})]_{\boldsymbol{r}=\boldsymbol{r'}}, \tag{2.10a}$$

$$J_{\mu\nu,\alpha}(\boldsymbol{r}) = \frac{1}{2i}[(\nabla_\mu - \nabla'_\mu)s_{\nu,\alpha}(\boldsymbol{r}, \boldsymbol{r'})]_{\boldsymbol{r}=\boldsymbol{r'}}. \tag{2.10b}$$

4. Pairing density $\tilde{\rho}_\alpha(\boldsymbol{r})$:

$$\tilde{\rho}_\alpha(\boldsymbol{r}) = \tilde{\rho}_\alpha(\boldsymbol{r}, \boldsymbol{r}). \tag{2.11}$$

For each of these local densities, isoscalar ($T = 0$) and isovector ($T = 1$) densities are introduced. For example, isoscalar and isovector kinetic densities are defined as

$$\tau_0(\boldsymbol{r}) = \tau_n(\boldsymbol{r}) + \tau_p(\boldsymbol{r}), \quad \tau_1(\boldsymbol{r}) = \tau_n(\boldsymbol{r}) - \tau_p(\boldsymbol{r}), \tag{2.12}$$

respectively. Then, each term in Eq. (2.4) can be specified as a functional of these local densities.

### 2.2.2 Skyrme EDF formalism

The kinetic energy density can be written as:

$$\mathcal{H}_{\mathrm{Kin}}(\boldsymbol{r}) = \frac{\hbar^2}{2m}\left(1 - \frac{1}{A}\right)\tau_0(\boldsymbol{r}), \tag{2.13}$$

where $\left(1 - \frac{1}{A}\right)$ stems from a simple approximation to the center-of-mass correction [81].

The interaction energy density is derived from the Skyrme effective nuclear potential

[72, 73], and can be written as [80]

$$\mathcal{H}_{\rm Int}(\boldsymbol{r}) = \sum_{t=0,1} (\chi_t^{\rm even}(\boldsymbol{r}) + \chi_t^{\rm odd}(\boldsymbol{r})), \tag{2.14}$$

where the isospin index, $t$, labels isoscalar ($t = 0$) and isovector ($t = 1$) densities (for a detailed derivation of the interaction energy density, one can refer to the appendix in [82]). The $\chi^{\rm even}$ and $\chi^{\rm odd}$ terms generate the time-even and time-odd mean fields, respectively [80]:

$$\chi_t^{\rm even}(\boldsymbol{r}) \equiv C_t^{\rho}\rho_t^2 + C_t^{\Delta\rho}\rho_t\Delta\rho_t + C_t^{\tau}\rho_t\tau_t + C_t^{J}\overset{\leftrightarrow}{J}{}_t^2 + C_t^{\nabla J}\rho_t\boldsymbol{\nabla}\cdot\boldsymbol{J}_t, \tag{2.15a}$$

$$\chi_t^{\rm odd}(\boldsymbol{r}) \equiv C_t^{s}\boldsymbol{s}_t^2 + C_t^{\Delta s}\boldsymbol{s}_t\cdot\Delta\boldsymbol{s}_t + C_t^{T}\boldsymbol{s}_t\cdot\boldsymbol{T}_t + C_t^{j}\boldsymbol{j}_t^2 + C_t^{\nabla j}\boldsymbol{s}_t\cdot(\boldsymbol{\nabla}\times\boldsymbol{j}_t). \tag{2.15b}$$

The coupling constant $C_t^{\rho}$ contains a density dependent term, which is written as

$$C_t^{\rho} = C_{t0}^{\rho} + C_{tD}^{\rho}\rho^{\gamma}. \tag{2.16}$$

Thus, the standard Skyrme interaction energy density is defined by means of the following parameters:

$$\begin{aligned} &\{C_t^{\rho}, C_t^{\Delta\rho}, C_t^{\tau}, C_t^{J}, C_t^{\nabla J}\}_{t=0,1} \\ &\{C_t^{s}, C_t^{\Delta s}, C_t^{T}, C_t^{j}, C_t^{\nabla j}\}_{t=0,1} \quad \text{and} \quad \gamma. \end{aligned} \tag{2.17}$$

One should note that when time reversal symmetry is conserved, the time-odd terms vanish.

The pairing channel can be parametrized by a density-dependent delta-pairing force with mixed volume and surface features [83],

$$V_{\rm pair}^{(n,p)} = V_0^{(n,p)}\left(1 - \frac{1}{2}\frac{\rho_0(\boldsymbol{r})}{\rho_c}\right)\delta(\boldsymbol{r} - \boldsymbol{r'}), \tag{2.18}$$

where $V_0^{(n,p)}$ is the pairing strength for neutrons ($n$) and protons ($p$), $\rho_0(\boldsymbol{r})$ is the isoscalar local density, and $\rho_c$ is the saturation density, fixed at $\rho_c = 0.16$ fm$^{-3}$. The resulting pairing energy density can be written as [78]

$$\mathcal{H}_{\text{pairing}}(\boldsymbol{r}) = \sum_{\alpha=n,p} \frac{V_0^\alpha}{2}\Big[1 - \frac{1}{2}\frac{\rho_0(\boldsymbol{r})}{\rho_c}\Big]\tilde{\rho}_\alpha^2(\boldsymbol{r}), \tag{2.19}$$

where $\tilde{\rho}$ is the local pairing density.

The Coulomb energy can be divided into the direct term, $\mathcal{H}_{\text{Coul}}^{\text{Dir}}$, and exchange term, $\mathcal{H}_{\text{Coul}}^{\text{Exc}}$. The direct term takes the usual form

$$\mathcal{H}_{\text{Coul}}^{\text{Dir}}(\boldsymbol{r}) = \frac{e^2}{2}\int d\boldsymbol{r}_1 \frac{\rho_p(\boldsymbol{r})\rho_p(\boldsymbol{r}_1)}{|\boldsymbol{r}-\boldsymbol{r}_1|}, \tag{2.20}$$

and the exchange term is usually calculated in the Slater approximation [84, 85]:

$$\mathcal{H}_{\text{Coul}}^{\text{Exc}}(\boldsymbol{r}) = -\frac{3}{4}e^2\Big(\frac{3}{\pi}\Big)^{1/3}\rho_p^{4/3}. \tag{2.21}$$

So far, the Skyrme EDF formalism has been presented. By fitting parameters (2.17) to selected experiment data, the following Skyrme functionals have been optimized:

- SkM* [86]
- SkP [87]
- SLy4 [88]
- SV-min [89]
- UNEDF0 [78]
- UNEDF1 [90]
- UNEDF1-HFB [91]
- UNEDF2 [92].

Of these, the UNEDF family was optimized in the framework of Hartree-Fock-Bogoliubov theory, which considers the mean-field and pairing channel simultaneously.

## 2.3 Mean-field methods based on nuclear DFT

Given the energy functional, one can construct the g.s. density using the Kohn-Sham theorem [93], which states that for any many-body interacting system, there exists a non-interacting system with a Kohn-Sham potential $V_{\mathrm{KS}}$, which gives the same density as the original system. The question is, given an EDF, how can one build the Kohn-Sham potential?

We assume that the Hamiltonian of the original system and the one-body Kohn-Sham potential can be written as

$$\hat{H} = \hat{T} + \hat{V} + \hat{U}_{\mathrm{ext}}, \tag{2.22}$$

$$\begin{aligned} \hat{H}_{\mathrm{KS}} &= \sum_{i=1}^{A} \hat{h}(\alpha_i), \alpha_i = \{\boldsymbol{r}_i, \boldsymbol{S}_i, \boldsymbol{t}_i\}, \\ \hat{h} &= \hat{t} + \hat{v}_{\mathrm{KS}}, \end{aligned} \tag{2.23}$$

respectively.

In the Kohn-Sham approximation, the single particle wave functions and energies can be obtained by solving the one-body Schrödinger equation:

$$\hat{h}\varphi_i = \varepsilon_i \varphi_i, \tag{2.24}$$

and the g.s. wave function of the system $|\Phi\rangle$ can be represented as a Slater determinant of single particle orbitals with the lowest energies. The corresponding one-body density is given by,

$$\rho_0(\boldsymbol{r}) = \sum_{i=1}^{A} |\varphi_i(\boldsymbol{r})|^2. \tag{2.25}$$

If the g.s. wave function for the original interacting system is $|\Psi\rangle$, then the g.s. energy

becomes:

$$\begin{aligned} E_0 &= \langle\Psi|\hat{H}|\Psi\rangle \\ &= \langle\Phi|\hat{H}|\Phi\rangle + (\langle\Psi|\hat{H}|\Psi\rangle - \langle\Phi|\hat{H}|\Phi\rangle) \\ &= \langle\Phi|\hat{T}|\Phi\rangle + \langle\Phi|\hat{V}|\Phi\rangle + \langle\Phi|\hat{U}_{\mathrm{ext}}|\Phi\rangle + (\langle\Psi|\hat{T}+\hat{V}|\Psi\rangle - \langle\Phi|\hat{T}+\hat{V}|\Phi\rangle). \end{aligned} \tag{2.26}$$

Here, we introduce:

$$T = \langle\Phi|\hat{T}|\Phi\rangle\,, \tag{2.27a}$$

$$E_{\mathrm{H}} = \langle\Phi|\hat{V}|\Phi\rangle\,, \tag{2.27b}$$

$$E_{\mathrm{ext}} = \langle\Phi|\hat{U}_{\mathrm{ext}}|\Phi\rangle\,, \tag{2.27c}$$

$$E_{\mathrm{xc}} = \langle\Psi|\hat{T}+\hat{V}|\Psi\rangle - \langle\Phi|\hat{T}+\hat{V}|\Phi\rangle\,. \tag{2.27d}$$

Then,

$$E_0 = T + E_{\mathrm{H}} + E_{\mathrm{ext}} + E_{\mathrm{xc}}, \tag{2.28}$$

where $T$ is the kinetic energy of the non-interacting system and $E_{\mathrm{xc}}$ represents the exchange and correlation energies. Applying the variational principle:

$$\begin{aligned} \delta E_0|_{\rho=\rho_0} &= \Big[\sum_i (\langle\delta\varphi_i|\hat{t}|\varphi_i\rangle + \langle\varphi_i|\hat{t}|\delta\varphi_i\rangle)\Big]|_{\rho=\rho_0} + (\delta E_{\mathrm{H}} + \delta E_{\mathrm{ext}} + \delta E_{\mathrm{xc}})|_{\rho=\rho_0} \\ &= \sum_i \varepsilon_i \delta\,\langle\varphi_i|\varphi_i\rangle - \Big[\int v_{\mathrm{KS}}\delta\rho d\boldsymbol{r}\Big]|_{\rho=\rho_0} + (\delta E_{\mathrm{H}} + \delta E_{\mathrm{ext}} + \delta E_{\mathrm{xc}})|_{\rho=\rho_0} \\ &= 0, \end{aligned} \tag{2.29}$$

One obtains:

$$\begin{aligned} v_{\rm KS} &= \frac{\delta E_{\rm ext}}{\delta\rho} + \frac{\delta E_{\rm H}}{\delta\rho} + \frac{\delta E_{\rm xc}}{\delta\rho} \\ &= U_{\rm ext} + v_{\rm H} + v_{\rm xc}. \end{aligned} \tag{2.30}$$

Therefore, given $E[\rho]$, the corresponding Kohn-Sham potential can be found by applying the variational principle. Then, by diagonalizing the resulting mean-field, one can construct the g.s. wave function, one-body density, and total energy using the Slater determinant based on the Kohn-Sham orbits.

### 2.3.1 Hartree-Fock and Hartree-Fock-Bogoliubov equations

The mean-field equations include the Hartree-Fock (HF) equations (which do not include pairing correlations) and the Hartree-Fock-Bogoliubov (HFB) equations (which account for the pairing channel). Variation of the Skyrme EDF with respect to $\rho$ and $\tilde{\rho}$ results in the Skyrme HFB equations [94]:

$$\begin{pmatrix} h & \tilde{h} \\ -\tilde{h}^* & -h^* \end{pmatrix} \begin{pmatrix} U_k \\ V_k \end{pmatrix} = \begin{pmatrix} U_k \\ V_k \end{pmatrix} E_k, \tag{2.31}$$

where $h$ is the HF field and $\tilde{h}$ is the pairing field:

$$h_n = -\frac{\hbar^2}{2m}\Delta + (\Gamma_0^{\rm even} + \Gamma_0^{\rm odd} + \Gamma_1^{\rm even} + \Gamma_1^{\rm odd}), \tag{2.32a}$$

$$h_p = -\frac{\hbar^2}{2m}\Delta + (\Gamma_0^{\rm even} + \Gamma_0^{\rm odd} - \Gamma_1^{\rm even} - \Gamma_1^{\rm odd}) + U^{\rm Coul}, \tag{2.32b}$$

$$\tilde{h}_q = V_0 \left(1 - V_1 \left(\frac{\rho}{\rho_0}\right)^{\gamma}\right) \tilde{\rho}_q. \tag{2.32c}$$

The momentum-dependent mean fields $\Gamma$ are given by [79, 95]

$$\Gamma_t^{\text{even}} = -\boldsymbol{\nabla}\cdot[M_t(\boldsymbol{r})\boldsymbol{\nabla}] + U_t(\boldsymbol{r}) + \frac{1}{2i}\left(\overleftrightarrow{\nabla}\sigma\cdot\overleftrightarrow{B}_t(\boldsymbol{r}) + \overleftrightarrow{B}_t(\boldsymbol{r})\cdot\overleftrightarrow{\nabla}\sigma\right), \tag{2.33a}$$

$$\Gamma_t^{\text{odd}} = -\boldsymbol{\nabla}\cdot[(\boldsymbol{\sigma}\cdot\boldsymbol{C}_t(\boldsymbol{r}))\,\boldsymbol{\nabla}] + \boldsymbol{\sigma}\cdot\boldsymbol{\Sigma}_t(\boldsymbol{r}) + \frac{1}{2i}\left(\boldsymbol{\nabla}\cdot\boldsymbol{I}_t(\boldsymbol{r}) + \boldsymbol{I}_t(\boldsymbol{r})\cdot\boldsymbol{\nabla}\right), \tag{2.33b}$$

where

$$U_t = 2C_t^{\rho}\rho_t + 2C_t^{\Delta\rho}\Delta\rho_t + C_t^{\tau}\tau_t + C_t^{\nabla J}\boldsymbol{\nabla}\cdot\boldsymbol{J}_t + U_t^{'}, \tag{2.34a}$$

$$\boldsymbol{\Sigma}_t = 2C_t^{s}\boldsymbol{s}_t + 2C_t^{\Delta s}\Delta\boldsymbol{s}_t + C_t^{T}\boldsymbol{T}_t + C_t^{\nabla j}\boldsymbol{\nabla}\times\boldsymbol{j}_t, \tag{2.34b}$$

$$M_t = C_t^{\tau}\rho_t, \tag{2.34c}$$

$$\boldsymbol{C}_t = C_t^{T}\boldsymbol{s}_t, \tag{2.34d}$$

$$\overleftrightarrow{B}_t = 2C_t^{J}\overleftrightarrow{J}_t - C_t^{\nabla J}\overleftrightarrow{\nabla}\rho_t, \tag{2.34e}$$

$$\boldsymbol{I}_t = 2C_t^{j}\boldsymbol{j}_t + C_t^{\nabla J}\boldsymbol{\nabla}\times\boldsymbol{s}_t. \tag{2.34f}$$

In Eq. (2.34a), the term $U_t^{'}$ represents the rearrangement terms resulting from the density dependence of the coupling constants.

For calculations with constraints, the Routhian $E^{'}$ is defined [80]:

$$E^{'} = E + E^{\text{mult}} + E^{\text{cran}} + E^{\text{numb}}, \tag{2.35}$$

i.e., equal to the sum of the energy and the terms responsible for constraints, here including the multipole, cranking and particle-number constraints.

For the multipole constraints, the standard quadratic form is taken:

$$E^{\text{mult}} = \sum_{\lambda\mu} C_{\lambda\mu}(\langle\hat{Q}_{\lambda\mu}\rangle - \bar{Q}_{\lambda\mu})^2, \tag{2.36}$$

where $\langle\hat{Q}_{\lambda\mu}\rangle$ are the average values of the mass-multipole-moment operator, $\bar{Q}_{\lambda\mu}$ are the constraint values of the multipole moments, and $C_{\lambda\mu}$ are the stiffness constraints.

The cranking constraints are assumed as the simple linear form:

$$E^{\text{cran}} = -\omega_y\langle\hat{J}_y\rangle, \tag{2.37}$$

where $\hat{J}_y$ is the operator of the component of the total angular momentum along the $y$ axis (due to the assumed symmetry in the codes used), $\bar{J}_y$ is the target value, and the rotational frequency $\omega_y$ is the corresponding Lagrange multiplier.

The particle-number constraints are given as

$$E^{\text{numb}} = -\lambda_n\langle\hat{N}_n\rangle - \lambda_p\langle\hat{N}_p\rangle, \tag{2.38}$$

which ensure the correct neutron and proton numbers. $\lambda_p$ and $\lambda_n$ are the neutron and proton Fermi energies.

Variation of the Routhian $E^{'}$ results in the constrained HFB equation, where the HF field in Eq. 2.31 is replaced by

$$h^{'} = h + 2\sum_{\lambda\mu} C_{\lambda\mu}(\langle\hat{Q}_{\lambda\mu}\rangle - \bar{Q}_{\lambda\mu})\hat{Q}_{\lambda\mu} - \omega_y\hat{j}_y - \lambda. \tag{2.39}$$

By solving the HFB equations, the resulting matrix $\mathcal{W}^\dagger$,

$$\begin{pmatrix} U^\dagger & V^\dagger \\ V^T & U^T \end{pmatrix}$$

transforms the particle operators $c^\dagger, c$ into the quasiparticle operators $\beta^\dagger, \beta$ through

$$\begin{pmatrix} \beta \\ \beta^\dagger \end{pmatrix} = \mathcal{W}^\dagger \begin{pmatrix} c \\ c^\dagger \end{pmatrix}.$$

Then the Hamiltonian $H$ can be approximated as

$$H = H^0 + \sum_k E_k \beta_k^\dagger \beta_k + \{\text{higher-order}\}. \tag{2.40}$$

The eigenstates of $H$ are the quasi-particle vacuum (with the energy $H^0$), one quasi-particle states with energies $H^0 + E_k$, two quasi-particle states, and so on.

Since the HFB equations are non-linear (due to the density-dependence of the mean-field potentials), they are often solved by iterative diagonalization methods. It is worth noting that, due to the self-consistent symmetry of the HFB equations, if some certain symmetry is expected in the solution, one should always start from a density initialized with this symmetry. This limits the size of model space and reduces the computational effort.

## 2.4 Nuclear DFT solvers

Solving the HF and HFB equations for complex exotic nuclei or nuclei with super-deformed configurations can be both difficult and time-consuming. In this dissertation, two DFT

solvers, HFODD and HFBTHO, have been employed:

1. HFBTHO [94, 96]

   HFBTHO solves the HFB equations in the cylindrical harmonic oscillator (HO) basis or in the transformed HO basis obtained by applying a local scale transformation [97, 98] on the HO functions. It implements all the general Skyrme functionals, and is able to do multiple constraint calculations. However, axial and time-reversal symmetries are explicitly imposed here.

2. HFODD [1, 80, 99–103]

   HFODD is more versatile than HFBTHO. It solves the HF, HF+BCS and HFB equations in the HO basis with the Skyrme, Gogny or Yukawa force, and it allows one to break all geometric and time reversal symmetries. HFODD has been employed to perform numerous calculations, such as constrained cranking calculations [104] and studies of spontaneous fission at finite temperatures [7].

Both solvers have been augmented with Open Multi-Processing (OpenMP) and Message Passing Interface (MPI) routines.

# Chapter 3

# Rotation of Triaxial Nuclei

## 3.1 Introduction

Among the predicted triaxial nuclei, neutron-rich Mo and Ru isotopes with $A \approx 110$ are of the most interest, as they exhibit shape changes and shape-coexistence phenomena [105]. With increasing neutron number, triaxial deformations are expected to appear in their ground states due to the occupation of the $1\nu h_{11/2}$ and $1\pi g_{9/2}$ intruder orbitals [33].

Experimentally, the clearest signature of triaxial shapes comes from the $\gamma$-ray spectroscopy of rotating nuclei. Since evidence for rotational-like behavior in the very neutron-rich even-even Zr-Pd region was reported in [106], there have been numerous experiments devoted to shape transitions and rotational properties of nuclei in this region. For example, the deformed configurations in $^{103,104,107}$Zr and $^{107,108}$Mo were studied in [107], and a transition from spherical to triaxial shapes in $^{104}$Ru was studied in [108]. After that, more and more evidence for triaxial deformation in neutron-rich Mo and Ru isotopes started to appear, including (i) the steady decrease of the $\gamma$-band band-head energy in $^{110}$Ru and $^{112}$Ru [109]; (ii) the collective triaxial behavior of Ru and Mo isotopes through the spectroscopy of fission fragments [2–4, 110–112]; (iii) the measurement of the quasi-$\gamma$ band in $^{110}$Mo [113, 114], and, (iv) the triaxial deformations in $^{104}$Ru and $^{110}$Mo extracted from $E2$ and $M1$ matrix elements obtained by Coulomb excitation studies [115].

Theoretically, triaxial ground states have been investigated with different models. For

example, in Ref. [33], triaxial g.s. minima were predicted in neutron-rich Mo isotopes with $N = 62$ - 66 using the macroscopic-microscopic approach. In Ref. [116, 117], the largest shell effects due to triaxial deformations were found around $^{108}$Ru. In Ref. [37, 38], potential energy surface calculations with HF and interacting boson models showed shallow triaxial minima for isotopes with $N = 64$ - 70. In Ref. [36], self-consistent HFB calculations with the Gogny D1S interaction predicted triaxial deformations for the even-even isotopes $^{104}$ - $^{110}$Mo and $^{104,106}$Ru. These different predictions come from the extreme softness of triaxial potential energy surfaces of nuclei in this region.

In the first project, motivated by the new experimental results for the transition quadrupole moments of rotational bands [6], we used nuclear DFT with the EDF UNEDF0 [78] to describe yrast structures in Mo and Ru isotopes. Our calculations predict triaxial g.s. deformations for $^{106,108}$Mo and $^{108,110,112}$Ru, and transition quadrupole moments that are consistent with experiment [29].

Triaxially deformed nuclei can execute not only principal-axis-cranking (PAC), where the rotation is about one of the principal axes, but also tilted-axis-cranking (TAC) [19, 118], where the rotational axis tilts away from the principal axis (PA). The standard theoretical model to describe collective rotation is the cranking model, in which the cranking term, $-\omega_1 J_1$ [18, 32, 119], is added to the mean-field Hamiltonian. In self-consistent PAC calculations, the nucleus is guaranteed to stay in the PA system. However, in TAC calculations, spurious processional motion has to be prevented by adding linear constraints, which give zero off-diagonal matrix elements of the inertia tensor. As shown by Kerman and Onishi [120], the corresponding Lagrange multipliers depend on the rotational frequencies, angular momenta and quadrupole moments of the system, and the actual relation is given by Eq. (3.6) in [120] and (3.10) below.

In the second project, with the proper linear constraints, we first verified the Kerman-Onishi condition in self-consistent mean-field calculations. We have shown that the solver-adapted Lagrange multiplier is consistent with the Kerman-Onishi condition to high precision. I then applied this result in PAC and TAC calculations with linear constraints for $^{160}$Yb [104] using the Skyrme HF approach (similar to the calculations for $^{158}$Er [121]). As an illustrative example, below I shall explain the nature of two TSD bands of $^{160}$Yb and also predict the possible large-amplitude collective motion at high spins.

## 3.2 Triaxial deformation

Before we can investigate nuclear shapes and their associated collective motion, we need to introduce the parametrization of the nuclear surface, which is given in terms of the length of a radius vector pointing from the origin to the surface [122]:

$$R = R(\theta, \phi) = R_0 \Bigg( 1 + \alpha_{00} + \sum_{\lambda=1}^{\infty} \sum_{\mu=-\lambda}^{\lambda} \alpha^*_{\lambda\mu} Y_{\lambda\mu(\theta,\phi)} \Bigg), \tag{3.1}$$

where $R_0$ is the radius of a sphere with the same volume. The quadrupole shapes are described by five parameters $\alpha_{2\mu}$. By a suitable rotation, one can transform to the body-fixed system characterized by three axes, which coincide with the principal axes of the mass distribution. Five quadrupole deformation parameters can be thus reduced to two independent quadrupole variables $\alpha_{20}$ and $\alpha_{22}$ and three Euler angles. For convenience, the so-called Bohr quadrupole deformations are introduced through

$$\begin{aligned} \alpha_{20} &= \beta_2 \cdot \cos\gamma, \\ \alpha_{22} &= \frac{1}{\sqrt{2}} \cdot \beta_2 \cdot \sin\gamma. \end{aligned} \tag{3.2}$$

In HFODD, the multipole moments are defined as

$$Q_{\lambda\mu} = a_{\lambda\mu} \cdot \frac{3A}{4\pi} \cdot R_0^{\lambda} \cdot \alpha_{\lambda\mu}, \tag{3.3}$$

where $A$ is the mass number, $R_0$ can be approximated as $\sqrt{5/3}\,\langle r^2\rangle^{1/2}$, where $\langle r^2\rangle^{1/2}$ is the r.m.s. radius, $a_{20} = \sqrt{16\pi/5}$ and $a_{22} = \sqrt{32\pi/5}$ [1]. By combining Eq. (3.2) and (3.3), one can get:

$$\beta_2 = \sqrt{\frac{\pi}{5}} \cdot \frac{1}{A\,\langle r^2\rangle} \cdot \sqrt{Q_{20}^2 + Q_{22}^2}, \tag{3.4a}$$

$$\tan\gamma = \frac{Q_{22}}{Q_{20}}, \tag{3.4b}$$

which will be used in the following. $\beta_2$ represents the elongation of the nucleus, and $\gamma$ is the triaxial deformation that ranges between $(0°, 60°)$ in the absence of rotation. Under rotation, $\gamma$ can be extended to the range of $(-120°, 60°)$.

## 3.3 Band crossing and angular momentum alignment

In the cranking model, the total Hamiltonian in the rotating reference frame can be written as

$$H^{\omega} = H - \omega_1 J_1. \tag{3.5}$$

By applying the variational principle in the rotating frame, the cranked HFB equation becomes

$$\begin{pmatrix} h - \lambda - \omega j_1 & \Delta \\ -\Delta^* & -h^* + \lambda + \omega j_1^* \end{pmatrix} \begin{pmatrix} U_k \\ V_k \end{pmatrix} = \begin{pmatrix} U_k \\ V_k \end{pmatrix} E_k^{\omega},$$

where $\omega$ is the rotational frequency, which is also the Lagrange multiplier to constrain the expectation value of the angular momentum. The $E_k^\omega$ can be referred to as the single quasiparticle Routhian energy.

As the rotational frequency $\omega$ increases, the single quasiparticle levels cross at some frequency $\omega = \omega^*$ (e.g. see Fig. 3.3). Beyond the crossing the vacuum configuration changes from the $g$-band (with the band-head in the g.s. configuration) to the $s$-band (with the band-head in the two quasi-particle configuration). The band crossing will lead to a sudden change in angular momentum.

In the next section, the shape changes and angular momentum alignment will be investigated for $^{106,108}$Mo and $^{108,110,112}$Ru.

## 3.4 Tilted-axis-cranking calculations and the Kerman-Onishi condition

In self-consistent HF TAC calculations, when the rotational axis moves away from the PA, the nucleus has to stay in the PA reference frame. This can be realized by adding linear constraints, which guarantee that the resulting off-diagonal matrix elements of the inertia tensor (or quadrupole moment) vanish. Using

$$\hat{Q}_{ij} \equiv x_i x_j, \tag{3.6}$$

the following condition should be fulfilled:

$$\langle \Phi | \hat{\boldsymbol{B}} | \Phi \rangle = 0 \quad \text{and} \quad \hat{B}_k = \hat{Q}_{ij} \ (i,j,k \text{ cyclic}). \tag{3.7}$$

Thus, the resulting Routhian can be written as

$$\hat{H}' = \hat{H} - \boldsymbol{\omega} \cdot \hat{\boldsymbol{J}} - \boldsymbol{\lambda} \cdot \hat{\boldsymbol{B}}, \tag{3.8}$$

where $\boldsymbol{\lambda}$ are three Lagrange multipliers, and the rotational frequencies $\boldsymbol{\omega}$ are determined from the angular-momentum condition:

$$\boldsymbol{J} = \langle \Phi | \hat{\boldsymbol{J}} | \Phi \rangle \, . \tag{3.9}$$

Kerman and Onishi proved that the Lagrange multipliers corresponding to linear constraints depend on angular momenta, rotational frequencies, and quadrupole moments [120]. This relation, referred to as the Kerman-Onishi condition in the following, is given by

$$\lambda_k = \frac{(\boldsymbol{\omega} \times \boldsymbol{J})_k}{D_i - D_j} \quad (i, j, k \text{ cyclic}), \tag{3.10}$$

where $D_i = \langle \Phi | \hat{D}_i | \Phi \rangle$ and $\hat{D}_i \equiv \hat{Q}_{ii}$. Consequently, nonzero values of $\boldsymbol{\lambda}$ imply that $\boldsymbol{\omega}$ and $\boldsymbol{J}$ are not parallel.

The Kerman-Onishi condition can also be written as:

$$-\lambda_1 x_2 x_3 = +\frac{\omega_2 j_3 - \omega_3 j_2}{\frac{\sqrt{3}}{6} \Re \langle Q_{22} \rangle + \frac{1}{2} \langle Q_{20} \rangle} \Im Q_{2-1} \equiv -L'_{2-1} \Im Q_{2-1}, \tag{3.11a}$$

$$-\lambda_2 x_1 x_3 = -\frac{\omega_3 j_1 - \omega_1 j_3}{-\frac{\sqrt{3}}{6} \Re \langle Q_{22} \rangle + \frac{1}{2} \langle Q_{20} \rangle} \Re Q_{21} \equiv -L'_{21} \Re Q_{21}, \tag{3.11b}$$

$$-\lambda_3 x_1 x_2 = -\frac{\omega_1 j_2 - \omega_2 j_1}{2 \Re \langle Q_{22} \rangle} \Im Q_{2-2} \equiv -L'_{2-2} \Im Q_{2-2}. \tag{3.11c}$$

In our calculations, we only allow the rotational axis to be tilted from the $x_2$ axis to

the $x_1$-$x_2$ plane. In this case, only one of the three constrains, $-L_{2-2}\Im Q_{2-2}$, is active. The other two constraints, $\langle \Im Q_{2-1} \rangle = 0$ and $\langle \Re Q_{21} \rangle$, are automatically met by enforcing $x_3$-$T$-simplex symmetry [123].

## 3.5 Project A: Triaxial rotation in the A $\approx$ 110 region

All the calculations for this project were performed with HFODD (version 2.49t) [103], and the wave functions were expanded in 800 spherical harmonic oscillator (HO) basis states with an oscillator frequency of $\hbar\omega = 49.2$ MeV/A$^{1/3}$. We have tested that such a basis provides a very reasonable precision for the observables studied.

In the particle-hole channel, we employed the global EDF UNEDF0 [78]. In the pairing channel, before the band crossing [18, 32], we took the zero-range density-dependent pairing force (2.18) with the Lipkin-Nogami correction for particle number fluctuations. The original pairing strengths were $(V_0^\nu, V_0^\pi) = (-170.374, -199.202)$ MeV fm$^3$, with a cutoff energy in the quasiparticle (q.p.) spectrum of $E_{\rm cut} = 60$ MeV. In the present calculation, the strengths of the pairing force for neutrons and protons were increased by 5% to produce the kinematic moment of inertia of the g.s. band of $^{106}$Mo. As discussed below, the potential energy surfaces (PES) are not sensitive to such a variation of pairing strengths. Beyond the band crossing, pairing was neglected in our calculation as the stating pairing correlations are reduced by angular momentum alignment; this is known as the Coriolis anti-pairing effect [124].

In multidimensional potential energy surface calculations, constraints are imposed on the expectation values of multiple moments. We used the augmented Lagrangian method [125] to perform the constrained iterations. The total Routhian calculations were computed within

the PAC approach [19].

### 3.5.1 Ground-state potential energy surfaces

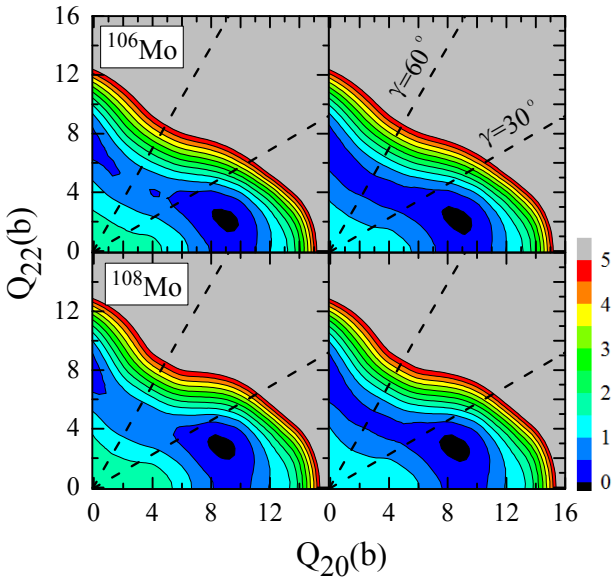


Figure 3.1: PES in the $(Q_{20}, Q_{22})$ plane in cranked HFB+UNEDF0 for $^{106}$Mo and $^{108}$Mo. Left: standard pairing strengths. Right: pairing strengths increased by 5%, see text. The difference between contour lines is 0.5 MeV.

Table 3.1: Bohr quadrupole deformation parameters $\beta_2$ and $\gamma$ calculated in HFB + UNEDF0 for the ground states of $^{106,108}$Mo and $^{108,110,112}$Ru.

| | $^{106}$Mo | $^{108}$Mo | $^{108}$Ru | $^{110}$Ru | $^{112}$Ru |
|---|---|---|---|---|---|
| $\beta_2$ | 0.19 | 0.18 | 0.16 | 0.16 | 0.15 |
| $\gamma$ | 16° | 18° | 24° | 25° | 24° |

We start the exploration of shape deformation with HFB calculations of g.s. potential energy surfaces for $^{106,108}$Mo and $^{108,110,112}$Ru. The results are shown in Fig. 3.1 and 3.2, respectively. In both figures, the left panels represent the results with the original pairing strengths, while the right panels show the results with increased pairing strengths. Triaxial deformed ground states are predicted in all cases. It turns out that a 5% change in the pairing strengths does not practically affect the PESs, causing only a slight increase

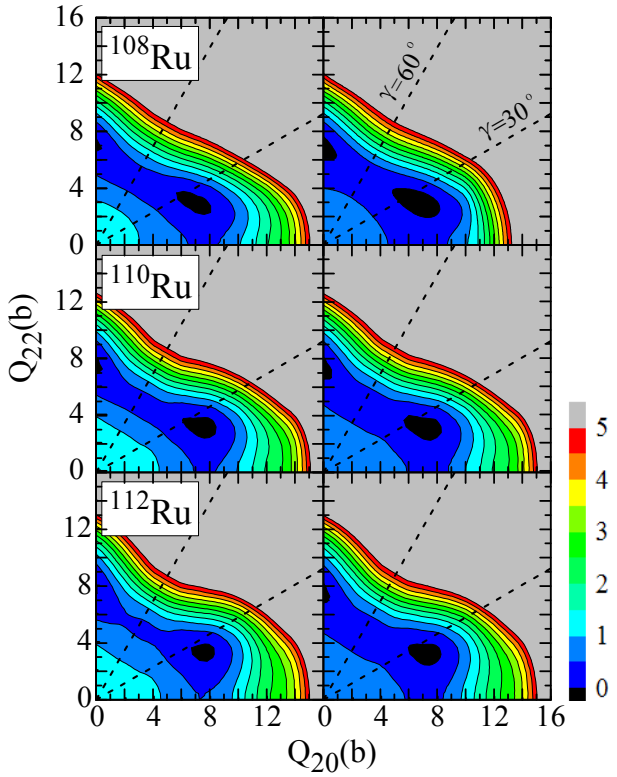


Figure 3.2: Similar to Fig. 3.1, but for $^{108}$Ru, $^{110}$Ru, and $^{112}$Ru.

in softness. In particular, the triaxial minima appearing at $(Q_{20}, Q_{22}) \approx (8.0\text{-}9.5, 2.0\text{-}3.0)$ b are hardly affected by pairing. The corresponding g.s. quadrupole deformations $(\beta_2, \gamma)$ are displayed in Table. 3.1. For $^{106,108}$Mo, we predicted the triaxial g.s. minima at $(\beta_2, \gamma) \approx (0.19, 17^\circ)$. Similar results were obtained in the macroscopic-microscopic calculations of Refs. [33,117,126] and HFB+D1S calculations [36]. For $^{108,110,112}$Ru, we also predict triaxial g.s. minima; this is consistent with Refs. [33, 127] and HF+SIII calculations of Ref. [109]. Triaxial g.s. shapes for $^{108,110}$Ru were also obtained in the survey [117] but $^{112}$Ru was calculated to be axial.

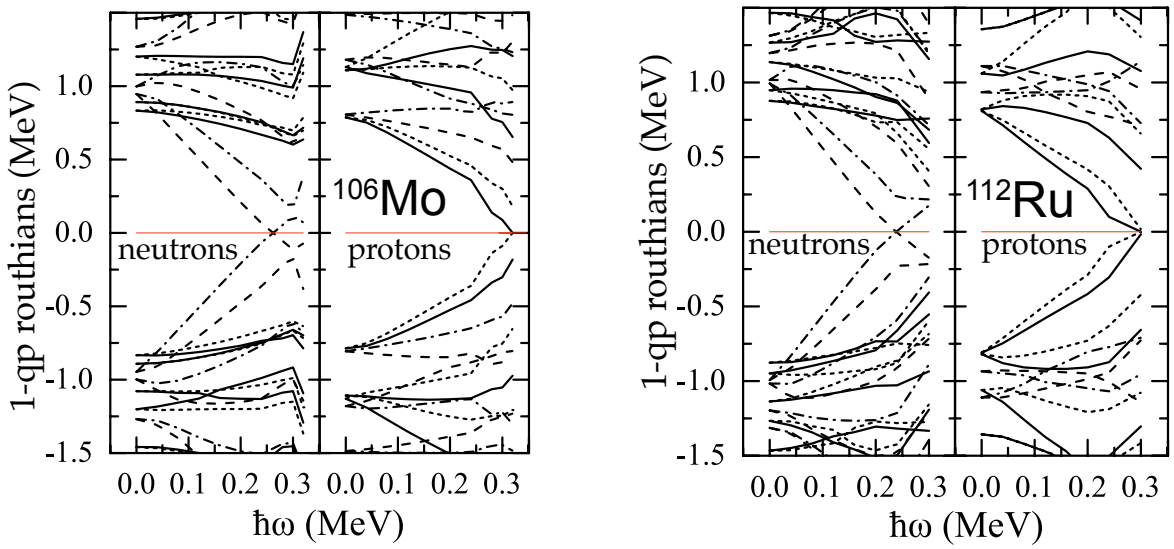


Figure 3.3: One-q.p. Routhian diagram for $^{106}$Mo (left) and $^{112}$Ru (right) obtained with cranked HFB+UNEDF0. The parity $\pi$ and signature $r$ (defined as the eigenvalue of $\hat{R}_y = \exp(-i\pi\hat{J}_y)$) of individual levels are indicated in the following way: $\pi = +, r = +i$ – solid line; $\pi = +, r = -i$ – dotted line; $\pi = -, r = +i$ – dot-dashed line; $\pi = -, r = -i$ – dashed line. The thin line indicates the Fermi energy.

### 3.5.2 Rotational properties

The angular momentum alignment pattern of Mo and Ru nuclei is governed by the $\nu h_{11/2}$ and $\pi g_{9/2}$ high-$j$ q.p. excitations, which give rise to strong shape polarization effects [33]. Figure 3.3 shows self-consistent cranked HFB+UNEDF0 1-q.p. Routhian diagrams versus rotational frequency for $^{106}$Mo and $^{112}$Ru, respectively. In both cases, the alignment of $\nu(h_{11/2})^2$ and $\pi(g_{9/2})^2$ pairs occurs at similar rotational frequencies of $\hbar\omega \approx 0.3$ MeV. At higher rotational frequencies, a transition is expected from the g.s. band configuration to aligned $\nu(h_{11/2})^2$ and $\pi(g_{9/2})^2$ 2-q.p. bands, and then to a 4-q.p. $\nu(h_{11/2})^2\pi(g_{9/2})^2$ band. These two consecutive crossings are difficult to follow in cranked HFB calculations, as this would require a diabatic-configuration extension [21, 32, 128] of the current framework. Such an extension is highly nontrivial in cranked HFB as the self-consistent mean-fields associated with aligned configurations are expected to differ significantly from those of the g.s.

band [33]. Moreover, pairing correlations in the aligned bands are quenched and this causes numerical instabilities around the band crossing. Therefore, to provide interpretation of the transition quadrupole moments at higher angular momenta, we carry out cranked Skyrme HF calculations without pairing at $\hbar\omega > 0.3$ MeV. In this case, diabatic configurations can be defined by the number of single-particle Routhians occupied in the four parity-signature blocks [100]. Specifically, each neutron and proton configuration is defined by four occupation numbers $[N_{++}, N_{+-}, N_{-+}, N_{--}]$ representing the number of particles $N_{\pi,r}$ occupying single-particle states of given $\pi$ and $r$. The lowest total Routhian with $\pi = +$ and $r = 1$ is associated with the yrast configuration.

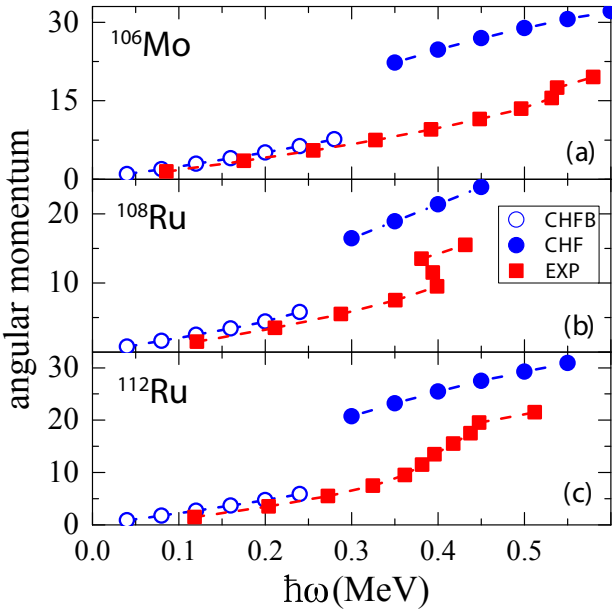


Figure 3.4: Angular momentum alignment for $^{106}$Mo and $^{108,112}$Ru. Cranked HFB ($\hbar\omega < 0.3$ MeV) and cranked HF ($\hbar\omega > 0.3$ MeV) calculations are compared to experiment [2–4]

The angular momentum alignment (total angular momentum as a function of rotational frequency) is shown in Fig. 3.4 for $^{106}$Mo, $^{108}$Ru, and $^{112}$Ru. Below the predicted band crossing at $\hbar\omega \approx 0.3$ MeV, our calculations reproduce experiment well. (Note, however, that our pairing strengths were adjusted to match the kinematic moment of inertia of $^{106}$Mo.)

The first band crossing, associated with the alignment of the $h_{11/2}$ neutron pair, is seen in $^{108,112}$Ru data slightly below $\hbar\omega = 0.4\,\mathrm{MeV}$, and is significantly delayed in $^{106}$Mo. The predicted aligned configuration above the band crossing has a fairly different shape as compared to that of the g.s. band, and it is difficult to follow the g.s. band at $\hbar\omega > 0.3\,\mathrm{MeV}$.

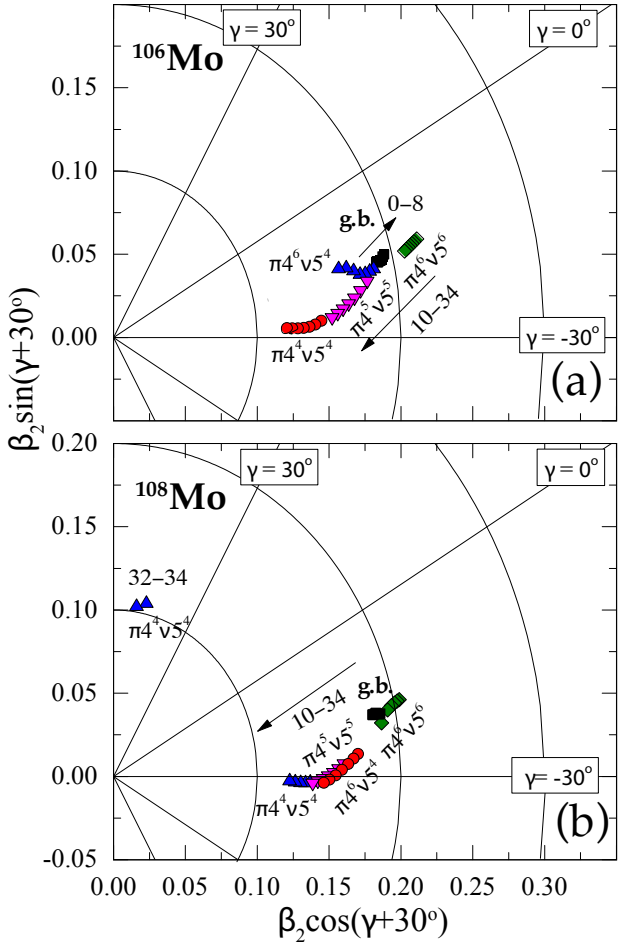


Figure 3.5: Summary of equilibrium deformations of the lowest $\pi = +, r = 1$ bands in $^{106,108}$Mo calculated with cranked HFB+UNEDF0 (ground band) and cranked HF+UNEDF0 (aligned bands). The rotational frequency is varied from zero to $\hbar\omega = 0.6\,\mathrm{MeV}$. The corresponding range of angular momentum is indicated. The aligned bands are classified according to the number of occupied high-$\mathcal{N}$ intruder levels ($\mathcal{N} = 5$ and 4 for neutrons and protons, respectively).

To investigate the evolution of nuclear shapes with rotation, we compute the equilibrium $\beta_2$ and $\gamma$ deformations for low-lying $\pi = +, r = 1$ bands in $^{106,108}$Mo (Fig. 3.5) and

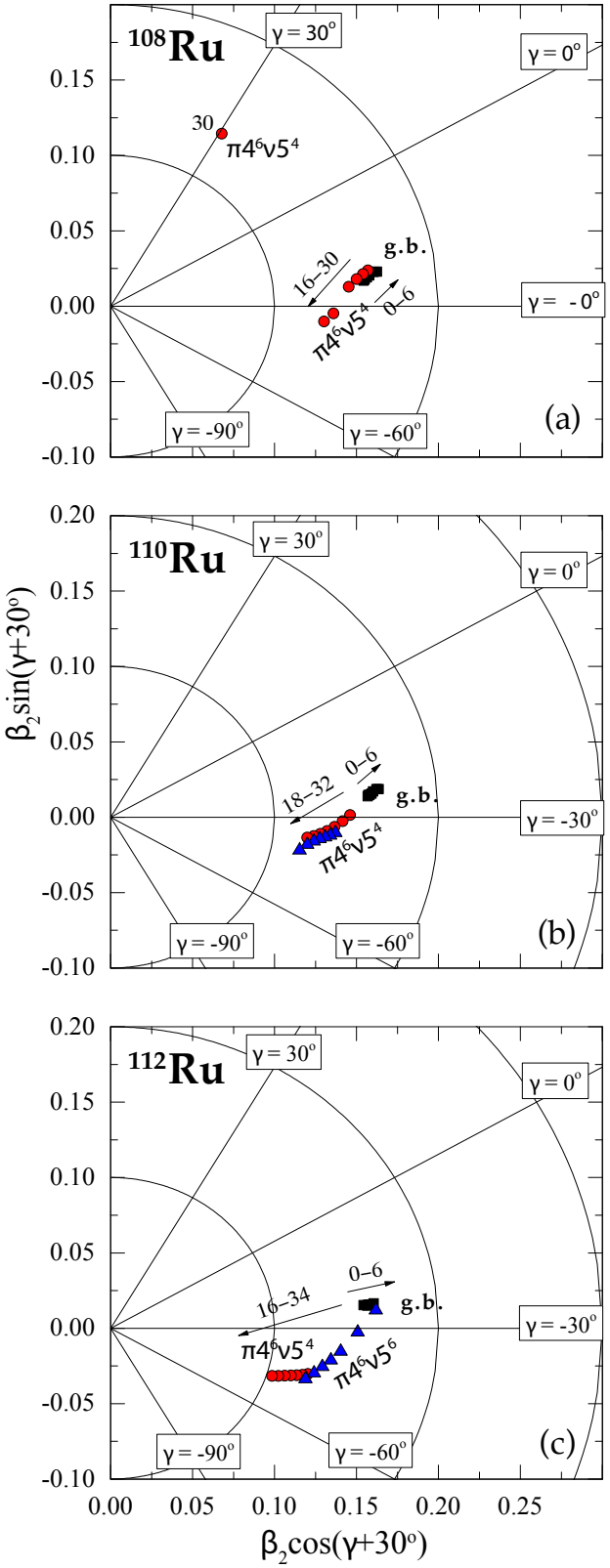


Figure 3.6: Similar to Fig. 3.5, but for $^{108,110,112}$Ru.

$^{108,110,112}$Ru (Fig. 3.6). In all cases considered, the triaxial paired g.s. band undergoes small centrifugal stretching in the direction of $\beta_2$. For instance, in the case of $^{108}$Ru, $\beta_2$ increases from the value of 0.15 at $\hbar\omega = 0$ to 0.17 at $\hbar\omega = 0.3\,\mathrm{MeV}$.

At higher spins ($10 \leq I \leq 36$), when pairing is neglected in our calculations, it is useful to label many-body configurations by the number of occupied intruder levels, i.e., $\mathcal{N}_{\mathrm{osc}} = 4$ protons (primarily $g_{9/2}$) and $\mathcal{N}_{\mathrm{osc}} = 5$ neutrons (primarily $h_{11/2}$). For instance, the aligned configuration $\pi(9,9,12,12) \otimes \nu(17,17,15,15)$ in $^{106}$Mo (shown by circles in Fig. 3.5(a)) can be denoted as $\pi 4^4 \nu 5^4$, and the same label applies to the $\pi(9,9,12,12) \otimes \nu(18,18,15,15)$ in $^{108}$Mo (shown by up-triangles in Fig. 3.5(b)).

The quadrupole deformations $\beta_2$ of aligned bands are predicted to be in the range of $0.12 \leq \beta_2 \leq 0.16$, which represents a reduction as compared to the shapes of paired ground-state bands. The aligned bands remain triaxial with $\gamma$ values around $-30^\circ$ up to $\hbar\omega = 0.6\,\mathrm{MeV}$. This finding is consistent with earlier results [33] which employed a cranked macroscopic-microscopic approach. At the highest rotational frequencies considered, our calculations predict the appearance of aligned triaxial configurations with $\gamma > 0$, which eventually terminate at oblate shapes ($\gamma \approx 60^\circ$), see, e.g., Fig. 3.5(b).

To study the stability of different triaxial minima at high spins, we analyze related diabatic total Routhians in the $(Q_{20}, Q_{22})$ plane. In Fig. 3.7 we show the total Routhian surfaces at $\hbar\omega = 0.5$ MeV for the selected low-lying aligned configurations in $^{106}$Mo discussed in Fig. 3.5(a). For all those configurations, the collective triaxial minimum with $\gamma$ between $-30^\circ$ and $-15^\circ$ appears lowest in energy. For the configuration $\pi 4^4 \nu 5^4$ shown in Fig. 3.7(a), we also predict a noncollective oblate state with $I = 34$ that represents a termination point of the $\gamma > 0$ band.

To eliminate spurious minima that are unstable with respect to the angular momentum

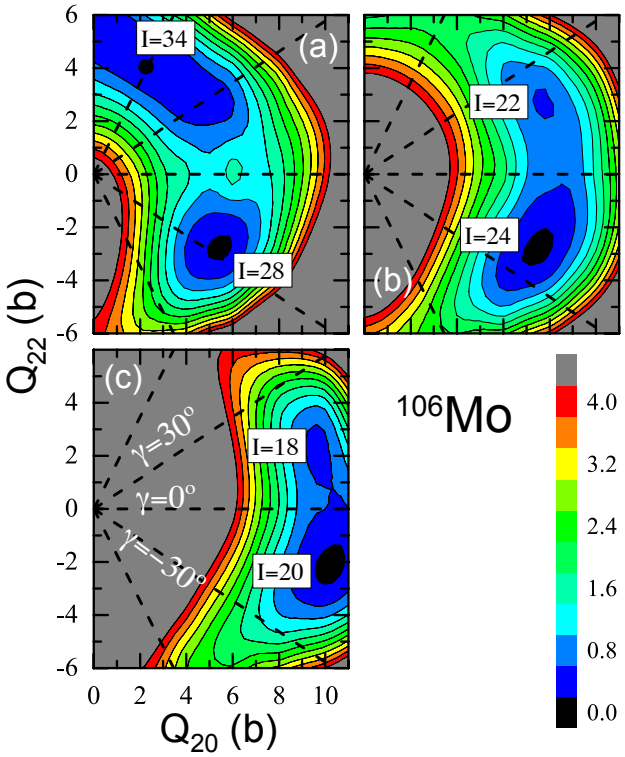


Figure 3.7: Diabatic total Routhian surfaces for $^{106}$Mo at $\hbar\omega = 0.5$ MeV calculated with CHF+UNEDF0 for the following configurations: (a) $\pi(9,9,12,12)\otimes\nu(17,17,15,15)$ ($\pi 4^4\nu 5^4$ in Fig. 3.5(a)); (b) $\pi(10,10,11,11)\otimes\nu(17,17,15,15)$ ($\pi 4^6\nu 5^4$); and (c) $\pi(10,10,11,11)\otimes\nu(16,16,16,16)$ ($\pi 4^6\nu 5^6$).

orientation, we also investigate the dependence of the Routhians on the angular momentum tilting angle $\theta$ with respect to the axis of rotation ($y$-axis). To this end, we used the TAC formalism of Refs. [104,121]. The calculations were performed for the aligned bands in $^{106}$Mo. At $\hbar\omega < 0.5\,$MeV, the total Routhians of triaxial ($\gamma < 0$) configurations $\pi 4^4\nu 5^4$, $\pi 4^5\nu 5^5$, and $\pi 4^6\nu 5^4$ of Fig. 3.5(a) show a minimum at $\theta = 0°$. At $\hbar\omega \approx 0.5\,$MeV, the Routhians become very soft in $\theta$, indicating a large-amplitude collective motion in this direction. This instability is not present for the $(\pi = -, r = 1)$ configuration $\pi(9,9,12,12)\otimes\nu(18,17,15,14)$ ($\pi 4^4\nu 5^5$), which shows a pronounced minimum at $\theta = 90°$ associated with $\gamma > 0$. This result is consistent with the deformation-driving effect of aligned $h_{11/2}$ neutrons orbitals discussed in Ref. [33].

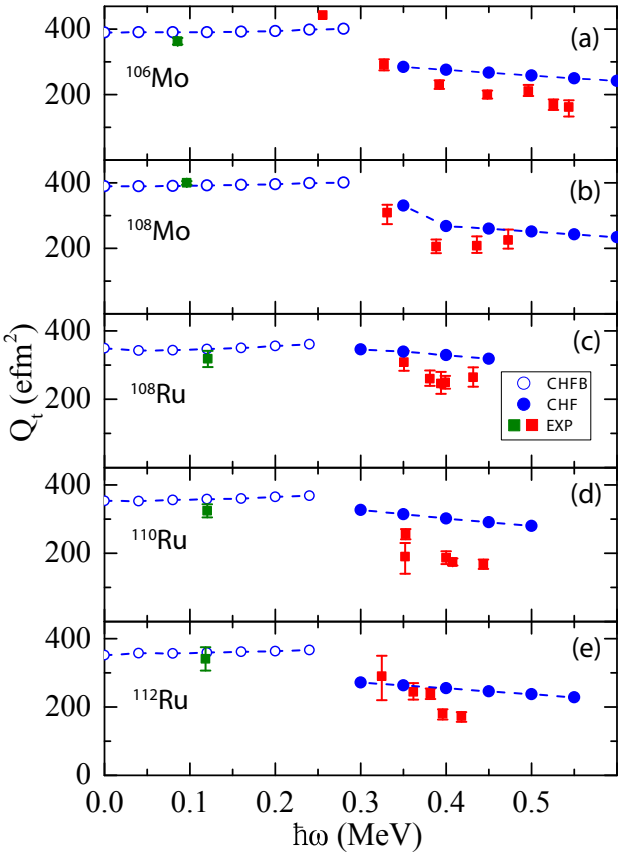


Figure 3.8: Transition quadrupole moments for $^{106,108}$Mo and $^{108,110,112}$Ru calculated in cranked HFB (open circles) and cranked HF (dots) compared to experiment. The $Q_t$ value at $I = 2$ is taken from Ref. [5] and the high-spin values from Ref. [6].

The transition quadrupole moments along the yrast band in $^{106,108}$Mo and $^{108,110,112}$Ru are shown in Fig. 3.8 as a function of rotational frequency. At low rotational frequencies $\hbar\omega < 0.3\,\mathrm{MeV}$, there is a gradual increase of $Q_t$ with $\omega$ due to the centrifugal stretching effect seen in Figs. 3.5 and 3.6. As discussed earlier, at higher frequencies cranking calculations are performed without pairing. While this approximation seriously affects the predicted angular momentum alignment shown in Fig. 3.4, the equilibrium shapes obtained in the cranked HF method are reasonable approximations to those obtained in the full cranked HFB framework [129,130], and reproduce experimental $Q_t$-values for aligned configurations [131,132]. As seen in Fig. 3.8, the predicted transition quadrupole moments in aligned bands

are slightly reduced with respect to the low-spin region due to the deformation reduction associated with the aligned $\nu h_{11/2}$ and $\pi g_{9/2}$ pairs. This reduction is generally consistent with experiment, except perhaps for $^{110}$Ru, where theory overestimates the measured $Q_t$ values above $\hbar\omega = 0.3\,\mathrm{MeV}$.

To further illustrate the importance of the $\gamma$ degree of freedom in the description of the band structures in the Mo and Ru isotopes, we have also carried out triaxial-projected-shell-model calculations for $^{106}$Mo with a range of $\gamma$ values. The obtained results, carried out by my collaborators, paint the same picture as cranked HFB and HF calculations, and strongly favor the triaxial interpretation [29].

## 3.6 Project B: Description of triaxial strongly deformed bands in $^{160}$Yb

In the previous section, TAC calculations have been performed for the aligned bands in $^{106}$Mo, but no details of this procedure were provided. In this section, to explain the experimentally observed TSD bands in $^{160}$Yb [133] and to illustrate the Kerman-Onishi condition, TAC calculations are performed with the cranked HF approach.

### 3.6.1 Tilted-axis-cranking calculations for $^{160}$Yb

The TAC calculations were performed by using the symmetry-unrestricted solver HFODD (version 2.49t). To be consistent with the previous work, we used the Skyrme EDF SkM* [86] and the wave function was expanded in 1000 deformed HO basis states with frequencies of $\hbar\Omega_x = \hbar\Omega_y = 10.080$ MeV (up to $N_x = N_y = 15$ HO quanta) and $\hbar\Omega_z = 7.418$ MeV (up to

$N_z = 20$ HO quanta).

Table 3.2: The configurations in $^{160}$Yb studied in this work. Each configuration is described by the numbers of occupied states in the four parity-signature $(\pi, r)$ blocks, in the convention of Ref. [1].

| Label | minimum | Configuration | parity |
|---|---|---|---|
| A | TSD1 | $\nu[23,23,22,22] \otimes \pi[16,18,18,18]$ | + |
| B | TSD1 | $\nu[23,24,21,22] \otimes \pi[16,18,18,18]$ | − |
| C | TSD1 | $\nu[23,24,21,22] \otimes \pi[18,18,17,17]$ | − |
| D | TSD3 | $\nu[23,23,22,22] \otimes \pi[18,18,17,17]$ | + |
| E | TSD3 | $\nu[23,23,22,22] \otimes \pi[17,17,18,18]$ | + |

For $^{160}$Yb, our calculations show that two competing PAC minima with similar values of $\beta_2$ and $|\gamma|$ but opposite values of $\gamma$ appear, which indicates unstable PAC solutions and thus the possible appearance of rotation along an axis which does not coincide with the PA. Therefore, before the TAC calculations, we first perform extensive PAC calculations so as to determine deformations of various minima. Similar to the PAC calculations in $^{158}$Er [134], we found that the configurations generally have three typical deformations, namely, $(Q_t, \gamma) \sim (9\ e\text{b}, 9°\text{-}14°)$ (TSD1), $(Q_t, \gamma) \sim (10.8\text{-}12.2\ e\text{b}, -10°)$ (TSD2), and $(Q_t, \gamma) \sim (10.0\text{-}10.5\ e\text{b}, 13°)$ (TSD3). Ranges of deformations indicate shape changes with rotational frequency.

Figure 3.9 shows the total Routhians of five configurations in $^{160}$Yb calculated with Skyrme HF as functions of the tilted angle, $\theta$, defined as the angle between the $x_2$-axis and the rotational axis in the $x_1$-$x_2$ plane. The corresponding configurations and parities are given in Table 3.2. At $\theta = 90°$, the $Q_{22}$ value changes sign and TSD1 becomes TSD2. It can be seen that, at $\omega = 0.5$ MeV, the Routhians of the bands A and B are very soft against $\theta$. For band A, even a minimum with $\theta \neq 0°$ or $90°$ develops. In such a situation, one may expect large-amplitude collective motion with a rotational axis that easily changes its direction. As the rotational frequency increases, the energy of the TSD2 bands increases

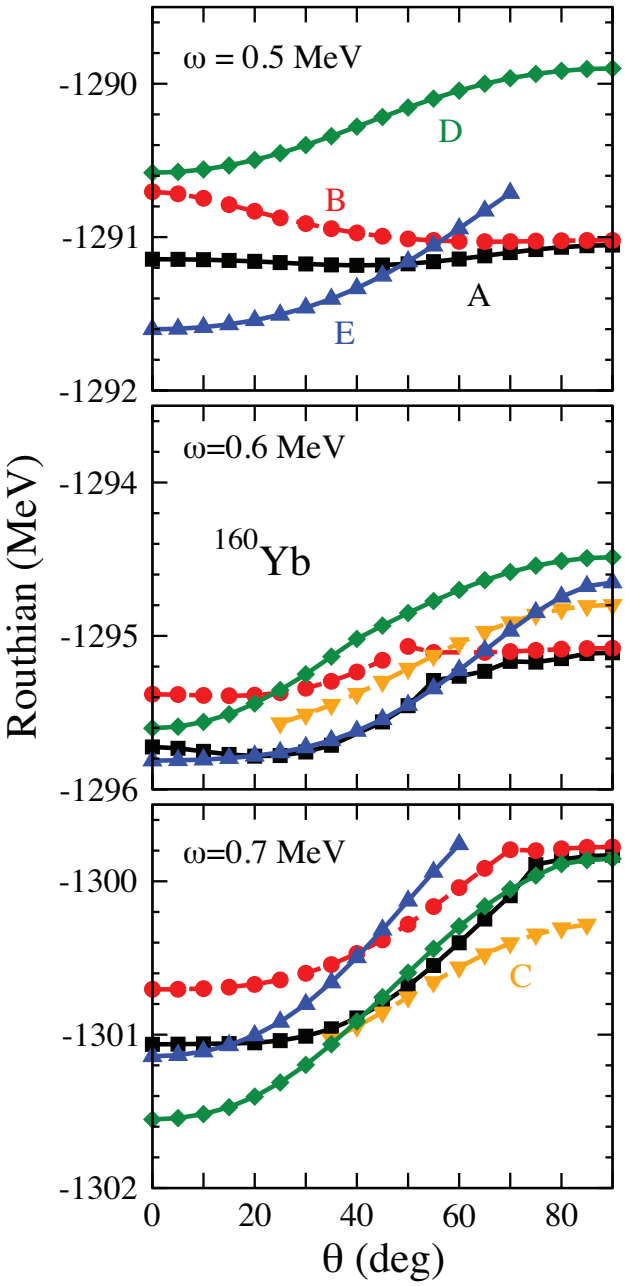


Figure 3.9: Total Routhians in $^{160}$Yb calculated within the SHF method as functions of the tilting angle $\theta$ for the five TSD configurations listed in Table 3.2. Solid and dashed lines mark configurations with positive and negative parity, respectively.

rapidly and these configurations become unphysical saddle points. At the same time, for the frequencies considered, the energies of the TSD3 bands are close to or even below the energies of the TSD1 and TSD2 bands.

## 3.7 Summary

In this chapter, we applied nuclear DFT to study triaxial shapes in the medium-heavy nuclei $^{106,108}$Mo and $^{108,110,112}$Ru, and TSD bands in $^{160}$Yb.

Triaxial g.s. deformations were predicted for $^{106,108}$Mo and $^{108,110,112}$Ru. Observed high-spin behavior of these nuclei is also consistent with triaxial rotation. However, the predicted triaxial ground state minima are fairly shallow, and this is perhaps why in some calculations, e.g., the cranked relativistic Hartree-Bogoliubov model of Ref. [6], axial configurations may be slightly favored. Particularly, in our work [29], the triaxial projected shell model was also employed to explain the observed band structures by assuming stable triaxial shapes, which has given consistent results with our nuclear DFT calculations.

In addition, with the Kerman-Onishi condition assumed, we employed the Skyrme HF method to perform TAC calculations for $^{160}$Yb. The results explained the nature of the TSD1 and TSD2 bands in $^{160}$Yb and predicted large-amplitude collective motion, which might appear at rotational frequency $\omega \approx 0.5$ MeV.

From mass distributions alone, multipole moments only tell us about geometric shapes of nuclei, leaving out detailed information on their shell structure. In the next chapter, we shall introduce the nucleon localization function, which also provides specific information on s.p. orbits.

# Chapter 4

# Nucleon Localization

## 4.1 Introduction

The degree of clustering in nuclei is difficult to assess quantitatively in DFT as the single particle wave functions are spread throughout the nuclear volume; hence, the resulting nucleonic distributions are rather crude indicators of cluster structures as their behavior in the nuclear interior is fairly uniform. Therefore, in this chapter, we utilize a different measure called spatial localization, which is a more selective signature of clustering and cluster shell structure. Spatial localization, originally introduced for the identification of localized electronic groups in atomic and molecular systems [22, 135–139], has recently been applied to characterize clusters in light nuclei [23]. This chapter is organized as follows: Sec. 4.2 gives an introduction to the spatial localization formalism, then two related projects are discussed in Sec. 4.3 and 4.4.

In the first project, to illustrate the basic concepts of nucleon localization, we employ the deformed harmonic oscillator (DHO) model and nuclear DFT to study cluster structures in deformed light nuclei. Then we apply this measure to track the development of fission fragments in heavy nuclei ($^{232}$Th, $^{264}$Fm and $^{240}$Pu) with their characteristic oscillation patterns [24, 31].

Spontaneous fission (SF) is a type of slow but large-amplitude collective motion, and only happens in heavy nuclei, which makes nuclear DFT an excellent tool to describe it.

As reported in previous work [7, 140–144], the fission pathway from the ground states of compound nuclei to separated fragments can be described by several collective coordinates (usually defined in terms of multipole moments), and may also be influenced by pairing and excitation energy. Therefore, determining the multi-dimensional PES is usually the first step of the calculation. Furthermore, since SF is a quantum process, all pathways should be considered theoretically with different probabilities [8]. These two considerations make SF calculations computationally expensive.

In the second project, we employ nuclear DFT to calculate both the density distribution and spatial localization distribution on the outer-turning line [140] and the scission line where fission happens for $^{240}$Pu. With the structure information obtained via spatial localization, fission fragments can be identified before scission.

## 4.2 Spatial localization

The spatial localization measure was originally introduced in atomic and molecular physics to characterize chemical bonds in electronic systems. It also turned out to be useful in visualizing cluster structures in light nuclei [23]. The localization measure can be derived by considering the conditional probabilities of finding a nucleon within a distance $\delta$ from a given nucleon at $\boldsymbol{r}$ with the same spin $\sigma$ ($\uparrow$ or $\downarrow$) and isospin $q$ ($n$ or $p$). As discussed in [22, 23], the expansion of this probability with respect to $\delta$ can be written as

$$R_{q\sigma}(\boldsymbol{r},\delta) \approx \frac{1}{3}\left(\tau_{q\sigma} - \frac{1}{4}\frac{|\boldsymbol{\nabla}\rho_{q\sigma}|^2}{\rho_{q\sigma}} - \frac{\boldsymbol{j}_{q\sigma}^2}{\rho_{q\sigma}}\right)\delta^2 + \mathcal{O}(\delta^3), \tag{4.1}$$

where $\rho_{q\sigma}$, $\tau_{q\sigma}$, $\boldsymbol{j}_{q\sigma}$, and $\boldsymbol{\nabla}\rho_{q\sigma}$ are the particle density, kinetic energy density, current density, and density gradient, respectively. A detailed derivation can be found in Appendix B. The densities have been defined in Sec. 2.2.1. By using the canonical basis [145], they can be re-expressed through the canonical HFB orbitals $\psi_\alpha(\boldsymbol{r}\sigma)$:

$$\begin{aligned}
\rho_{q\sigma}(\boldsymbol{r}) &= \sum_{\alpha\in q} v_\alpha^2 |\psi_\alpha(\boldsymbol{r}\sigma)|^2, && \text{(4.2a)}\\
\tau_{q\sigma}(\boldsymbol{r}) &= \sum_{\alpha\in q} v_\alpha^2 |\boldsymbol{\nabla}\psi_\alpha(\boldsymbol{r}\sigma)|^2, && \text{(4.2b)}\\
\boldsymbol{j}_{q\sigma}(\boldsymbol{r}) &= \sum_{\alpha\in q} v_\alpha^2 \mathrm{Im}[\psi_\alpha^*(\boldsymbol{r}\sigma)\boldsymbol{\nabla}\psi_\alpha(\boldsymbol{r}\sigma)], && \text{(4.2c)}\\
\boldsymbol{\nabla}\rho_{q\sigma}(\boldsymbol{r}) &= 2\sum_{\alpha\in q} v_\alpha^2 \mathrm{Re}[\psi_\alpha^*(\boldsymbol{r}\sigma)\boldsymbol{\nabla}\psi_\alpha(\boldsymbol{r}\sigma)], && \text{(4.2d)}
\end{aligned}$$

with $v_\alpha^2$ being the canonical occupation probability. Thus, the expression in the parentheses of Eq. (B.6) can serve as a localization measure. Unfortunately, this expression is neither dimensionless nor normalized. A natural choice for normalization is the Thomas-Fermi kinetic energy density $\tau_{q\sigma}^{\mathrm{TF}} = \frac{3}{5}(6\pi^2)^{2/3}\rho_{q\sigma}^{5/3}$. Considering that the spatial localization and $R_{q\sigma}$ are in an inverse relationship, a dimensionless and normalized expression for the localization measure can be written as

$$\mathcal{C}_{q\sigma}(\boldsymbol{r}) = \left[1 + \left(\frac{\tau_{q\sigma}\rho_{q\sigma} - \frac{1}{4}|\boldsymbol{\nabla}\rho_{q\sigma}|^2 - \boldsymbol{j}_{q\sigma}^2}{\rho_{q\sigma}\tau_{q\sigma}^{\mathrm{TF}}}\right)^2\right]^{-1}. \tag{4.3}$$

In our work, time reversal symmetry is conserved and $\boldsymbol{j}_{q\sigma}$ vanishes.

A value of $\mathcal{C}$ close to one indicates that the probability of finding two nucleons with the same spin and isospin at the same spatial location is very low. Thus the nucleon's localization is large at that point. In particular, nucleons making up the alpha particle are perfectly localized [23]. Another interesting case is $\mathcal{C} = 1/2$, which corresponds to a homogeneous

Fermi gas as found in nuclear matter. When applied to many-electron systems, the quantity $\mathcal{C}$ is referred to as the electron localization function, or ELF. In nuclear applications, the measure of localization (4.3) shall thus be called the nucleon localization function (NLF).

The above definition of the NLF works well in regions with non-zero nucleonic density. When the local densities become very small in regions outside the range of the nuclear mean field, numerical instabilities can appear. On the other hand, when the particle density is close to zero, localization is no longer a meaningful quantity. Consequently, for finite nuclei, we multiply the NLF by a normalized particle density $\mathcal{C}(\boldsymbol{r}) \to \mathcal{C}(\boldsymbol{r})\rho_{q\sigma}(\boldsymbol{r})/[\max(\rho_{q\sigma}(\boldsymbol{r}))]$.

## 4.3 Project C: Nucleon localization in nuclei

In this project, we employed the axial DHO model and nuclear DFT. For the light nuclei discussed in Sec. 4.3.2, where pairing can be neglected, we solved the constrained HF problem with the functional UNEDF1-HFB [91] (except for the discussion in octupole deformed $^{20}$Ne. For details, see Sec. 4.3.2). In the discussion of fissioning heavy nuclei in Sec. 4.3.3, pairing correlations are important. Therein, we solved the constrained HFB problem with the UNEDF1 functional optimized for fission [90] in the presence of pairing treated by means of the Lipkin-Nogami approximation as in Ref. [146]. Both HFBTHO [96] and HFODD [103] were used to solve the HF and HFB equations.

### 4.3.1 NLFs within the axial harmonic oscillator model

Since the average potential in light nuclei can be fairly well approximated by that of a deformed HO [147–149], many properties of these systems can be characterized in terms of the HO shell structure. Quantum mechanically, the unusual stability of cluster states

in light nuclei can be attributed to strong shell effects that are present in deformed single particle orbitals. Indeed, in the deformed HO model the strongest level degeneracy occurs when the ratio of oscillator frequencies is a rational number; this results in the appearance of supershells [70, 148, 149]. Consequently, the deformed HO model can serve as a rough guide to describe cluster states [61, 64, 70, 150]. To this end, we first study the NLFs using the wave functions of the axial HO with frequencies $\omega_\perp$ and $\omega_z$. For the integer values of $\eta \equiv \omega_\perp/\omega_z$ (prolate shapes), a supershell structure appears that is associated with the $\eta$-fold SU(3) dynamical symmetry of the rational HO [70]. For instance, for $\eta = 2$, the superdeformed magic numbers are $2, 4, 10, 16, \ldots$, etc. For oblate shapes, the degeneracy pattern of the rational HO is different [151]. For instance for $\eta = 0.9$ the magic numbers are $2, 6, 8, 14, \ldots$ [149,151]. In the examples below for $N = Z$ nuclei, we only show densities and NLFs for one combination of spin and isospin as time-reversal and isospin symmetries are conserved.

In Fig. 4.1 we show particle densities and NLFs for superdeformed configurations in $^8$Be and $^{20}$Ne with $\eta = 2$, and for an oblate configuration in $^{12}$C with $\eta = 0.9$. All of these configurations correspond to closed shells of the deformed HO. In the case of $^8$Be, both the density and the NLF reveal two clear centers. The NLF values at these centers are close to one, which means that the nucleons are highly localized, implying the presence of $\alpha$ clusters. For $^{20}$Ne, the cluster structure is difficult to see in the particle density plot. However, the NLF clearly demonstrates the presence of two $\alpha$ clusters at the tips and a ring structure around $z = 0$ associated with an oblate-deformed $^{12}$C nucleus. Figures 4.1(e) and (f) indeed show that the $\eta = 0.9$ configuration in $^{12}$C exhibits a very similar localization pattern, except that the localization level is higher. This is easy to understand as the wave functions of $\alpha$ clusters in $^{20}$Ne have a non-zero overlap with the ring structure of $^{12}$C, and this decreases

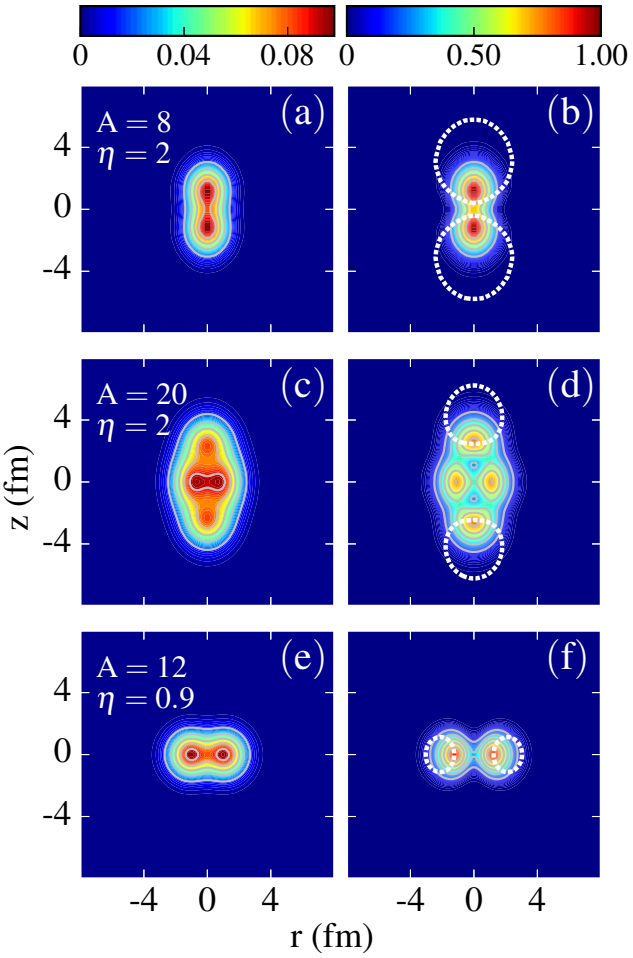


Figure 4.1: Left: particle density $\rho_{n\uparrow}$ (in nucleons/fm$^3$) for prolate configurations in $^8$Be and $^{20}$Ne with $\eta = 2$, and for an oblate configuration in $^{12}$C with $\eta = 0.9$. Right: corresponding masked NLFs as described in Sec. 4.2. White dotted lines are the contour lines $\mathcal{C} = 0.9$ of the original definition (4.3).

the level of localization.

In Fig. 4.2, we show three more examples of elongated configurations in $^{36}$Ar, $^{16}$O and $^{24}$Mg. In the first row, we show a hyperdeformed ($\eta = 3$) configuration in $^{36}$Ar. While the particle density hardly shows clustering, the localization shows large values, especially at the tips of the nucleus. The structure in between corresponds to a deformed $^{28}$Si and also exhibits cluster structures at $z = 0$ and $z \approx \pm 2$ fm. The white dotted line represents the $\mathcal{C} = 0.9$ contour of the original localization measure. In the second and third rows, in order

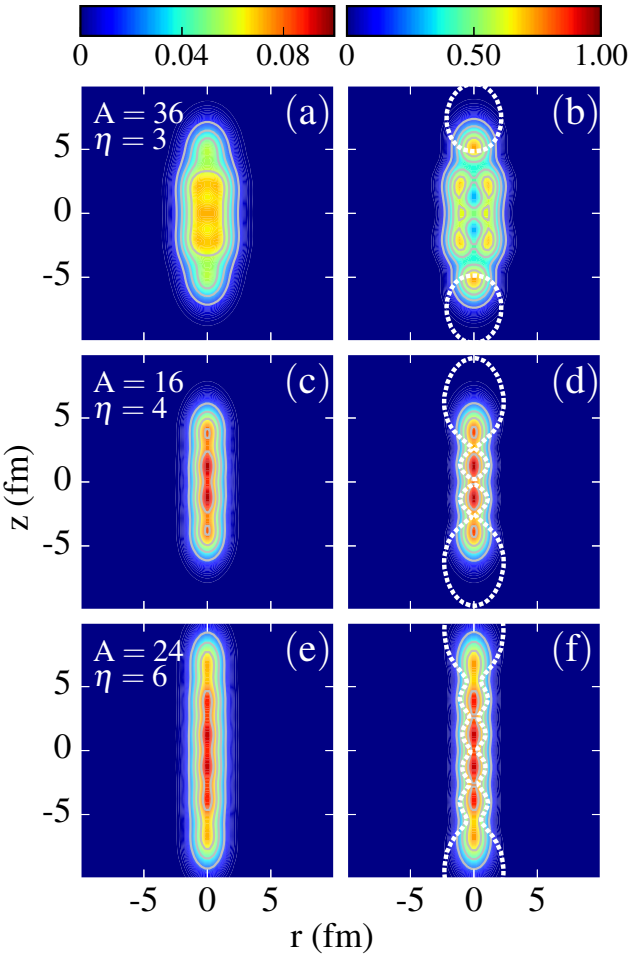


Figure 4.2: Similar to Fig. 4.1, but for $^{36}$Ar, $^{16}$O and $^{24}$Mg.

to simulate $\alpha$-chain configurations, we choose $\eta$ according to the $\alpha$ particle content. While a separation into $\alpha$ particles is difficult to see in the particle density plot, especially for $^{24}$Mg, the NLF clearly reveals four maxima for $^{16}$O and six maxima for $^{24}$Mg, with localizations close to one. This means that the nucleons are very localized for each spin/isospin component, implying the presence of $\alpha$-chain configuration.

### 4.3.2 NLFs in light nuclei

In order to compare the deformed HO results with a realistic nuclear model, we carry out nuclear DFT calculations for $^{8}$Be, $^{20}$Ne and $^{36}$Ar. For light nuclei with $N = Z$, results for

neutrons and protons are very similar as the Coulomb contribution is small. Therefore, we only consider neutron densities and spin-up NLFs. Figures 4.3, 4.4 and 4.5 show our results of constrained HF calculations with UNEDF1-HFB assuming good parity.

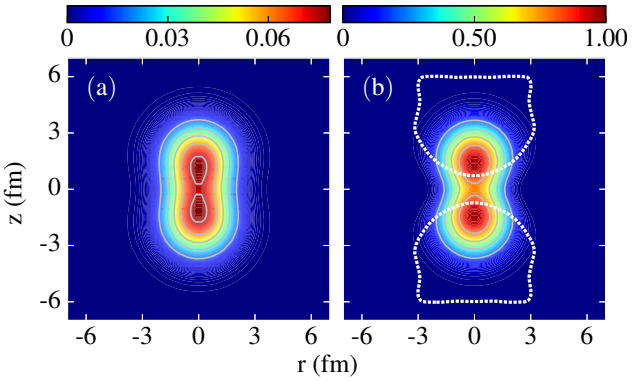


Figure 4.3: Left: neutron density $\rho_n$ (in nucleons/fm$^3$) for the HF ground-state of $^8$Be computed with the functional UNEDF1-HFB. Right: corresponding masked NLFs as described in Sec. 4.2. White dotted lines are the contour lines $\mathcal{C} = 0.9$ of the original definition (4.3).

Figure 4.3 depicts $\rho_n$ and $\mathcal{C}_{n\uparrow}$ for the ground-state configuration of $^8$Be. Both quantities are very similar to the HO results of Fig. 4.1(a) and (b), again revealing the presence of two $\alpha$ clusters.

Figure 4.4 shows HF results for $^{20}$Ne for both its axially deformed configuration with $\beta_2 \approx 0.38$ and a hyperdeformed minimum with $\beta_2 \approx 0.9$. The values of $\rho_n$ and $\mathcal{C}_{n\uparrow}$ at the first local minimum are similar to the HO results of Figs. 4.1(c) and (d). Again, the particle density does not show any pronounced cluster structure, while the spatial localization shows the presence of the $\alpha$-$^{12}$C-$\alpha$ structure. As the quadrupole deformation increases, the localization of the three clusters becomes more pronounced.

Our results for $^8$Be and $^{20}$Ne compare well with the HF-SkI3 calculations of Ref. [23]. In both cases, unmasked NLFs exhibit numerical artifacts in the low-density region, because the numerator and denominator in Eq. (4.3) are both close to zero.

Figure 4.5 shows the HF energy of $^{36}$Ar as a function of the quadrupole deformation

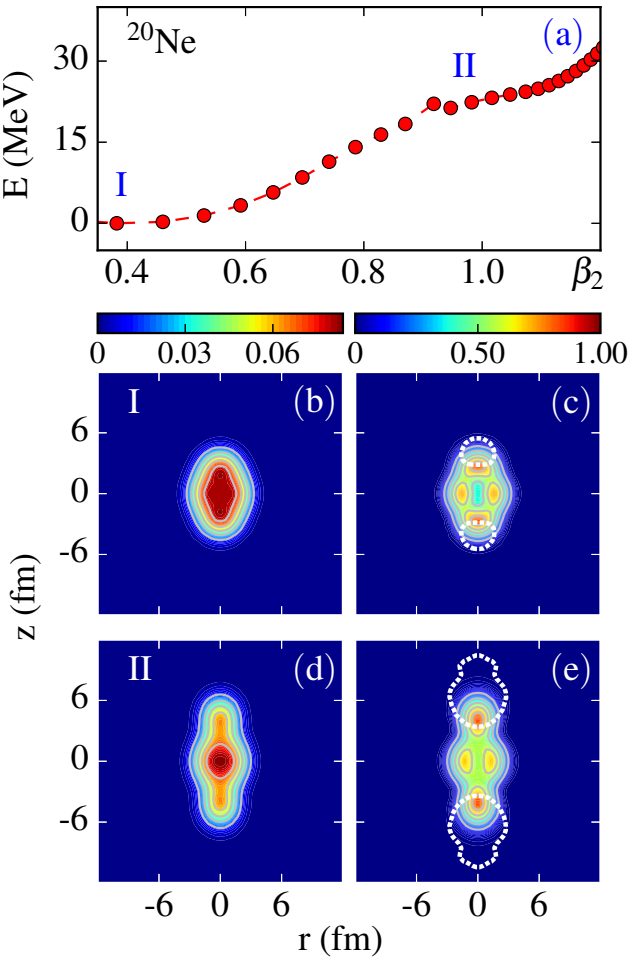


Figure 4.4: (a) Total HF energy of $^{20}$Ne versus quadrupole deformation parameter $\beta_2$. The predicted lowest minimum is normalized to 0. The neutron densities (in nucleons/fm$^3$) at the two local minima I and II are shown in panels (b) and (d), respectively, and the corresponding NLFs are plotted in panels (c) and (e).

$\beta_2$. The three local minima are predicted at $\beta_2 \approx 0.1$, 0.5, and 0.8. The corresponding neutron densities and NLFs are also displayed in Fig. 4.5 (clustering in $^{36}$Ar has also been studied in the DFT calculations of Ref. [68]). The weakly-deformed ground state at $\beta_2 \approx 0.1$ does not show any structure in the density. Its NLF exhibits a maximum in the center and an enhancement at the tips. This distribution constitutes a unique fingerprint of the shell structure of $^{36}$Ar that is clearly missing in the density plot. Configuration II is less deformed than that calculated with the HO in Fig. 4.2. However, its NLF is similar. In particular, the

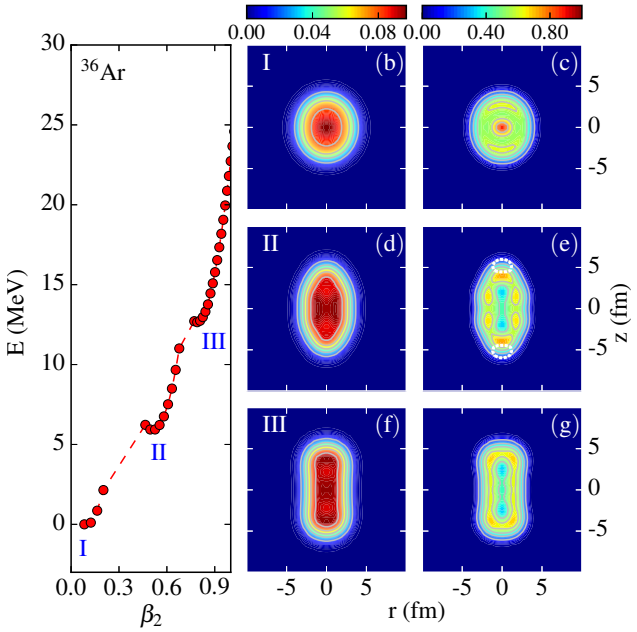


Figure 4.5: Similar to Fig. 4.4, but for $^{36}$Ar.

localization enhancement at the tips reveals the presence of alpha clustering. The central structure shows two rings of the enhanced surface localization. Unlike shape II, shape III has a more uniform NLF, with the localization peaked around the nuclear surface where the contribution from one specific single-particle orbital is likely to dominate.

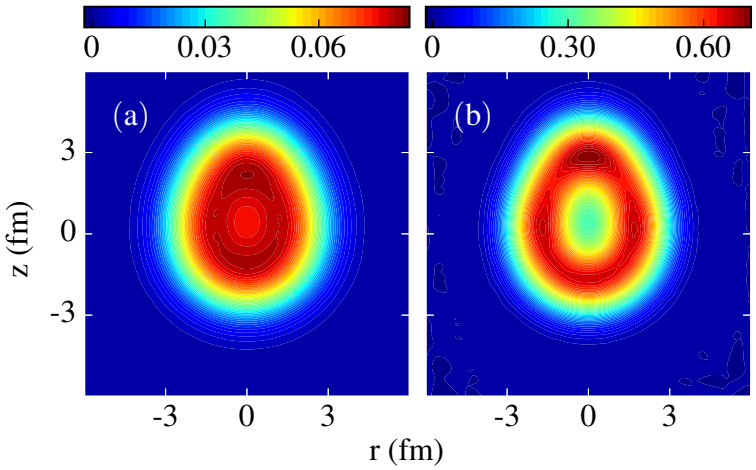


Figure 4.6: Similar to Fig. 4.3 but for the reflection-asymmetric ground state of $^{20}$Ne at $\beta_2 = 0.35$ and $\beta_3 = 0.57$.

If parity is not constrained in HF calculations, the ground state of $^{20}$Ne is expected

to be reflection-asymmetric [152]. In Refs. [153–155], the $K^\pi = 0^-$ configuration in $^{20}$Ne is predicted to have a cluster-like structure with a large octupole deformation, while the $K^\pi = 0^+$ ground state is situated between cluster-like and shell-like configurations. To illustrate this special case, we use HFODD to perform a constrained HFB calculation for $^{20}$Ne at the octupole deformation $\beta_3 \approx 0.57$ [155], which is benefical for obtaining the stable solution, while the pairing strengths chosen are very small. The octupole deformation $\beta_3$ is defined through the corresponding axial octupole moment $Q_{30}$: $\beta_3 = \frac{4\pi}{5}\sqrt{\frac{3}{5}}\frac{Q_{30}}{A\langle r^2\rangle^{3/2}}$. As seen in Fig. 4.6, the intrinsic configuration of $^{20}$Ne has a rather compact shape. A clear dip in the NLF at the center manifests a region where all wave functions overlap. A slight enhancement of the spatial localization near the tip is visible. While the ground-state of $^{20}$Ne shows a faint trace of an $\alpha$-$^{16}$O structure, the localization is rather low; hence, the quasimolecular picture does not apply for the UNEDF1-HFB Skyrme functional used.

### 4.3.3 NLFs in heavy nuclei

Based on the examples shown in the last section, we conclude that the NLF is an excellent tool for visualizing cluster structures in light nuclei. In this section, we will apply this tool to monitor the development and evolution of fission fragments in $^{232}$Th, $^{264}$Fm and $^{240}$Pu. Since the Coulomb interaction is significant in heavy nuclei, the isospin symmetry is broken. Therefore, both neutron and proton results will be discussed here.

Figure 4.7 shows the potential energy curves of $^{232}$Th and $^{240}$Pu along the most probable fission pathway predicted, respectively, in Refs. [7] and [8]. The calculations are performed with the UNEDF1 functional. Both curves show secondary minima associated with superdeformed fission isomers. For $^{232}$Th, a pronounced softness is observed at large quadrupole moments $Q_{20} \approx 150 - 200\,\mathrm{b}$. In this region of collective space, a hyperdeformed third

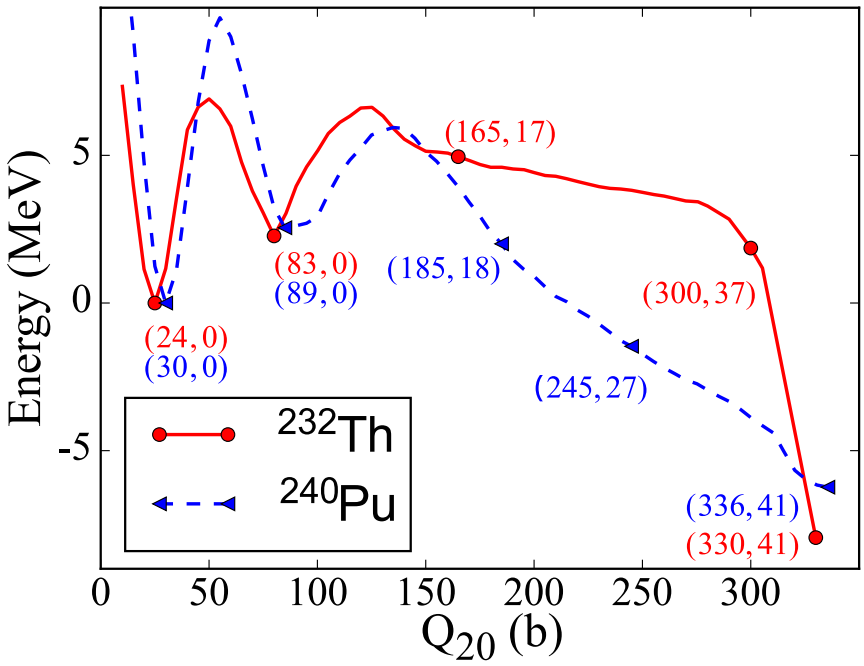


Figure 4.7: The potential energy curves of $^{232}$Th and $^{240}$Pu calculated with UNEDF1 along the fission pathways [7, 8]. The configurations further discussed in Figs. 4.8 and 4.12 are marked by symbols. Their quadrupole and octupole moments, $Q_{20}$(b) and $Q_{30}$ (b$^{3/2}$) respectively, are indicated.

minimum is predicted by some Skyrme functionals [7]. In the next step, we consider five configurations along the fission pathway to perform detailed localization analysis.

Figure 4.8 shows neutron and proton densities and NLFs for $^{232}$Th along the fission pathway. The first column corresponds to the ground-state configuration where the densities do not show obvious internal structures. However, the neutron NLF shows three concentric circles and the proton NLF exhibits two maxima and an enhancement at the surface. The second column corresponds to the fission isomer. Here two center distributions begin to form in both NLFs. As discussed in [7], the distributions shown in the third column can be associated with a quasimolecular "third-minimum" configuration, in which one fragment bears a strong resemblance to the doubly magic nucleus $^{132}$Sn. The fourth column represents the configuration close to the scission point, where two well-developed fragments are present.

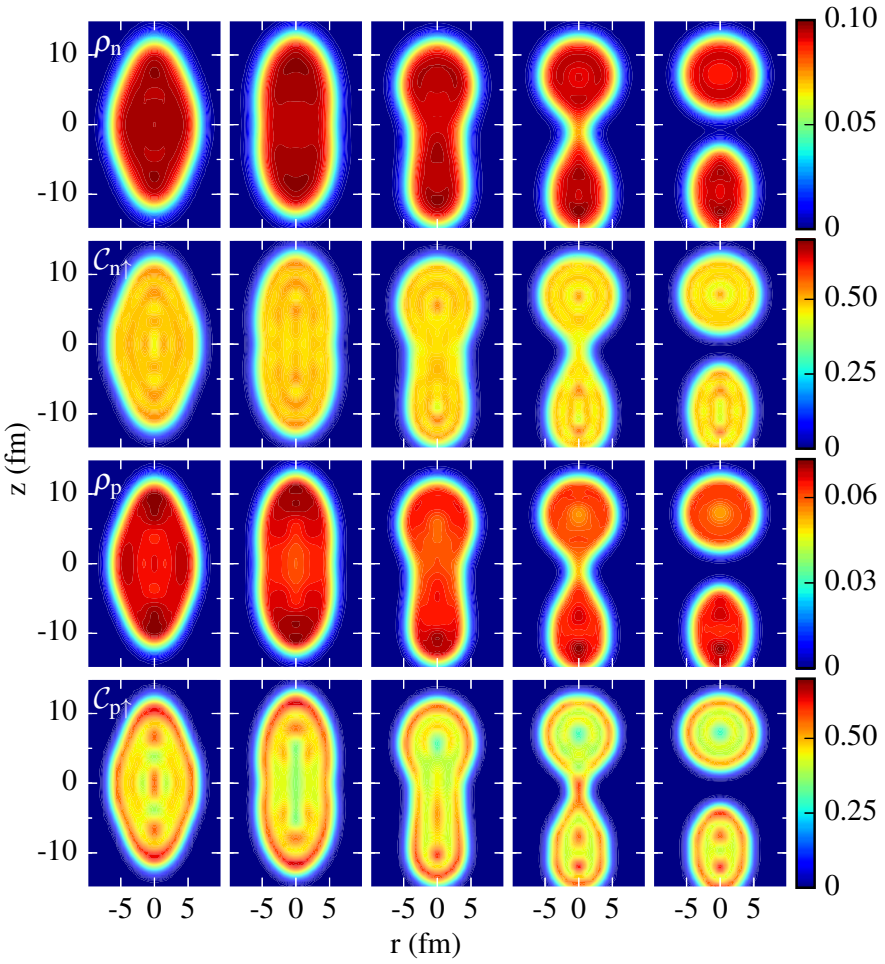


Figure 4.8: Nucleonic densities (in nucleons/fm$^3$) and spatial localizations for $^{232}$Th obtained from HFB calculations with UNEDF1 for five configurations along the fission pathway marked in Fig. 4.7.

As seen in the last column, at larger elongations beyond scission, the nucleus breaks up into two fragments, one spherical and another one strongly deformed.

To study the evolution of fission fragments, we performed HFB calculations for the presumed fission fragments $^{132}$Sn and $^{100}$Zr. The results are shown in Fig. 4.9.

The nucleus $^{132}$Sn is a doubly-magic system with a characteristic shell structure. Except for a small depression at the center of proton density in Fig. 4.9(c)(left), the nucleonic densities are almost constant in the interior. On the other hand, the NLFs show characteristic patterns of concentric rings with enhanced localization, in which the neutron NLF exhibits

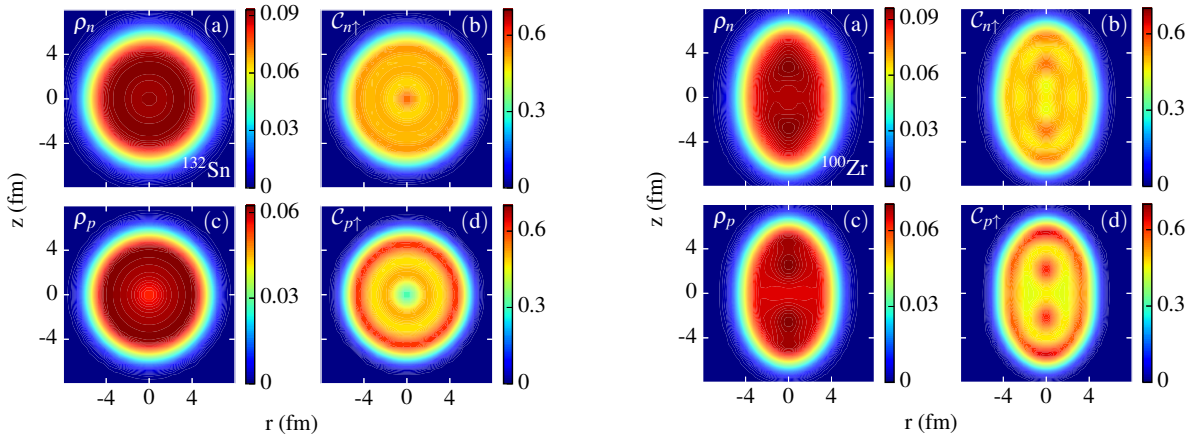


Figure 4.9: Nucleonic densities (in nucleons/fm$^3$) and spatial localizations for the ground state of $^{132}$Sn (left) and $^{100}$Zr (right).

.

one additional maximum as compared to the proton NLF; this is due to the additional closed neutron shell. As one can see, unlike in atomic systems [22], the total number of shells cannot be directly read from the number of peaks in the NLF, because the radial distributions of wave functions belonging to different nucleonic shells vary fairly smoothly and are poorly separated in space. Nevertheless, each magic number leaves a strong and unique imprint on the spatial localization.

For $^{100}$Zr , the calculation is performed at the prolate configuration with $Q_{20} = 10\,\mathrm{b}$, which corresponds to the lighter fission fragment predicted in [7]. Again, while the particle densities are almost constant in the interior, the neutron NLF shows two concentric rings and the proton NLF exhibits two centers in the interior and one enhanced ring at the surface.

The characteristic patterns seen in the NLFs of fission fragments can be spotted during the evolution of $^{232}$Th in Fig. 4.8. To show it more clearly, Fig. 4.10 displays the NLFs of the three most elongated configurations of $^{232}$Th along the $z$-axis in Fig. 4.8 and compares them to those of $^{132}$Sn and $^{100}$Zr. To avoid normalization problems we present NLFs given by Eq. (4.3), i.e., without applying the density form factor. In Figs. 4.10 (a) and (b), neutron

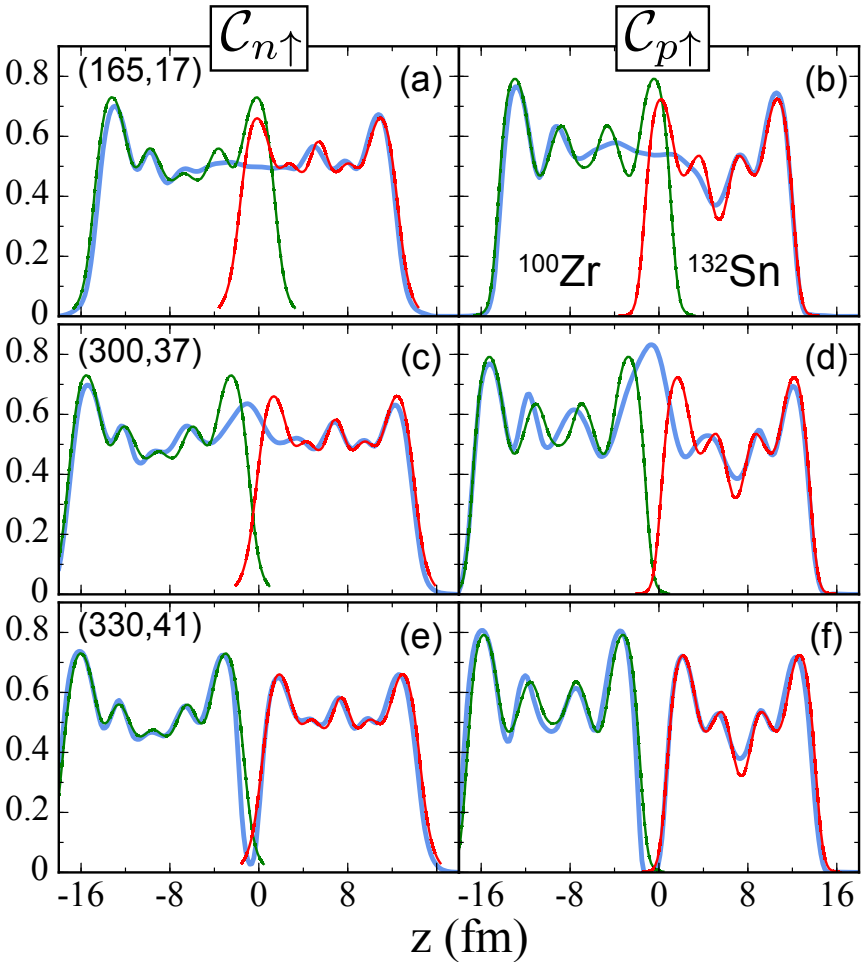


Figure 4.10: Neutron (left) and proton (right) NLF profiles for $^{232}$Th (blue thick line), $^{100}$Zr (green line), and $^{132}$Sn (red line) along the $z$ axis ($r = 0$). The first, second, and third panels correspond to the configurations in the third, fourth and fifth columns of Fig. 4.8, respectively.

and proton localizations at the center are around 0.5, which is close to the Fermi gas limit. This is expected for a fairly heavy nucleus. In the exterior, the localizations of two developing fragments match those of $^{100}$Zr and $^{132}$Sn fairly well. In panels (c) and (d), the NLFs of $^{232}$Th grow in the interior; this demonstrates that the nucleons become localized at the neck region. Finally, in panels (e) and (f), the fission fragments are separated and their NLFs are consistent with the localizations of $^{100}$Zr and $^{132}$Sn.

As another illustrative example, we show in Fig. 4.11 the distributions computed for

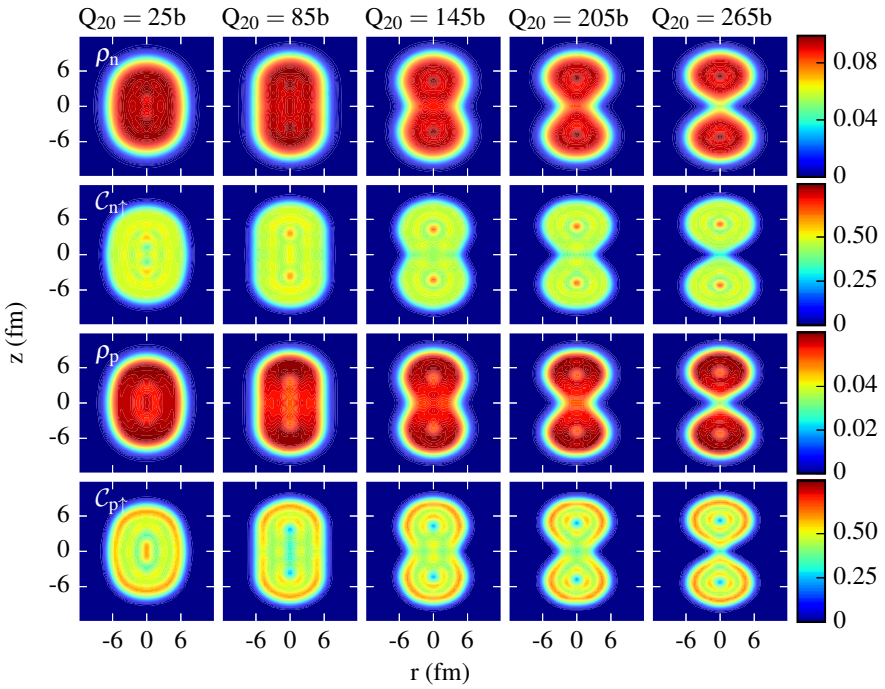


Figure 4.11: Similar to Fig. 4.8 but for the configurations of $^{264}$Fm. The quadrupole moments of the configurations are denoted on top of each column.

$^{264}$Fm, in which symmetric fission was predicted. As the constraining quadrupole moment $Q_{20}$ gets larger, the particle densities become increasingly elongated. A neck develops at $Q_{20} \approx 145$ b, and the scission point is reached at $Q_{20} \approx 265$ b above which $^{264}$Fm splits into two $^{132}$Sn fragments. By comparing to the results for $^{132}$Sn in Fig. 4.9, one can see the gradual development of the $^{132}$Sn clusters within the fissioning nucleus.

Finally, let us consider the important case of $^{240}$Pu. Recently, a microscopic modeling of mass and charge distributions in spontaneous fission of this nucleus was carried out in Ref. [8]. To give an insight into the evolution of $^{240}$Pu along its fission pathway, in Fig. 4.12 we illustrate the NLFs of $^{240}$Pu. The transition to the reflection-asymmetric pathway begins at $Q_{20} \approx 95$ b. It is seen that two nascent fragments start developing at this configuration. At larger elongations internal parity is broken and two fragments are formed with distinct shell imprints in the corresponding NLFs. In the last column, the rings of enhanced localization

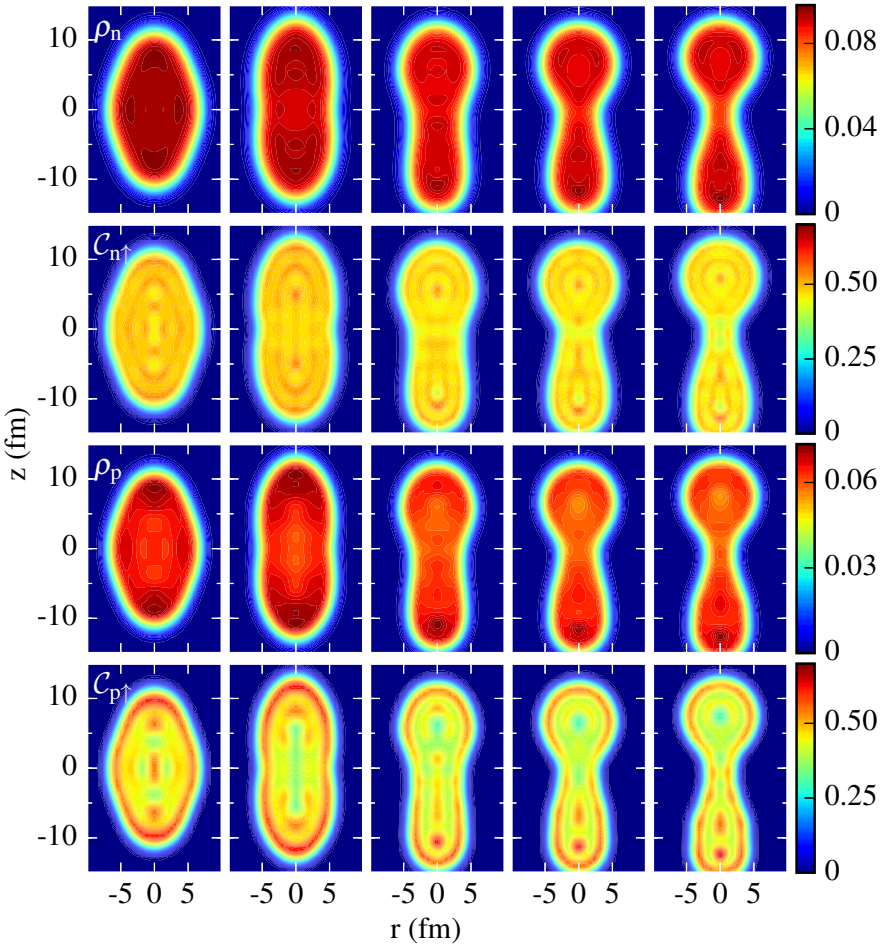


Figure 4.12: Similar to Fig. 4.8 but for the configurations of $^{240}$Pu indicated in Fig. 4.7.

are almost closed, and the fragments are nearly separated. Three examples, $^{232}$Th, $^{264}$Fm and $^{240}$Pu, show in a rather dramatic fashion that the NLFs can serve as excellent fingerprints of both the formation and evolution of cluster structures in fissioning nuclei.

## 4.4 Project D: Identifying fission fragments

In the previous section, nucleon spatial localization was employed to describe the clustering substructures in light and heavy nuclei successfully. In this project, it will be applied to identify fission fragments in $^{240}$Pu.

### 4.4.1 Fission fragment distribution

In a semi-classical approximation for spontaneous fission, the penetration probability from the inner-turning point, $A$, to the outer-turning point, $B$, is given by

$$P = (1 + \exp[2S(L)])^{-1}, \tag{4.4}$$

where $S(L)$ is the least action integral calculated along the one-dimensional fission path $L(s)$ preselected in the multidimensional collective space:

$$S(L) = \int_{s_{\rm A}}^{s_{\rm B}} \frac{1}{\hbar}\sqrt{2\mathcal{M}_{\rm eff}(s)(V_{\rm eff}(s) - E_0)}ds, \tag{4.5}$$

where $V_{\rm eff}(s)$ and $\mathcal{M}_{\rm eff}(s)$ are the effective potential energy and inertia along the fission path $L(s)$, respectively. $V_{\rm eff}$ can be obtained by subtracting the vibrational zero-point energy $E_{\rm ZPE}$ from the total HFB energy $E_{\rm tot}$. $E_{\rm ZPE}$ can be estimated by using the Gaussian overlap approximation [156]. Integral limits $s_A$ and $s_B$ are the classical inner and outer turning points, respectively, defined by $V_{\rm eff}(s) = E_0$ on the two extremes of the fission path. The collective ground state energy, $E_0$, was assumed to be equal to 1 MeV. $ds$ is the element of length along $L(s)$. The expression for $\mathcal{M}_{\rm eff}$ is [8, 157–159]

$$\mathcal{M}_{\rm eff}(s) = \sum_{ij} \mathcal{M}_{ij}\frac{dq_i}{ds}\frac{dq_j}{ds}, \tag{4.6}$$

where $\mathcal{M}_{ij}$ are the components of the multi-dimensional collective inertia tensor, which can be calculated by using the non-perturbative cranking approximation [160]. The $q_i$ are collective variables.

From outer-turning points to scission points, the time-dependent fission path can be approximated by solving the dissipative Langevin equations [161, 162]:

$$\begin{aligned} \frac{dp_i}{dt} &= -\frac{p_j p_k}{2}\frac{\partial}{\partial x_i}(\mathcal{M}^{-1})_{jk} - \frac{\partial V}{\partial x_i} - \eta_{ij}(\mathcal{M}^{-1})_{jk}p_k + g_{ij}\Gamma_j(t), \\ \frac{dx_i}{dt} &= (\mathcal{M}^{-1})_{ij}p_j, \end{aligned} \tag{4.7}$$

where $x_i = q_i/\delta q_i$ is the dimensionless coordinate, $\delta q_i$ is the scaling parameter [141, 160], $p_i$ represents the momentum conjugate to $x_i$, $\eta_{ij}$ is the dissipation tensor, $g_{ij}\Gamma_i(t)$ is the random (Langevin) force with $\Gamma_j(t)$ being a time-dependent stochastic variable with a Gaussian distribution, and $g_{ij}$ is the random-force strength tensor. This project is based on the work in [8], and use the same parameters defined therein.

### 4.4.2 Fragments identification for $^{240}$Pu

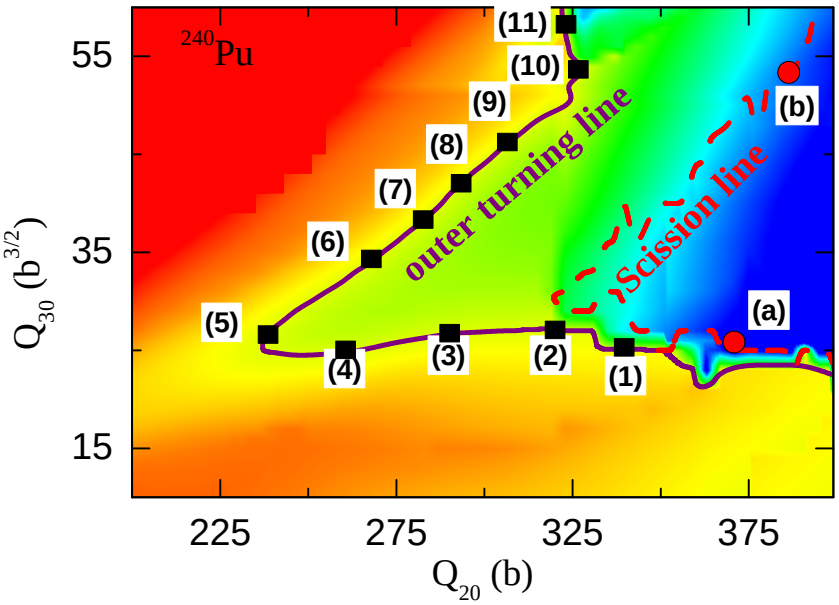


Figure 4.13: Outer turning line (thick solid line) and scission line (dashed line) on the potential energy surface of $^{240}$Pu. Symbols indicate the selected configurations for which subsequent results are shown.

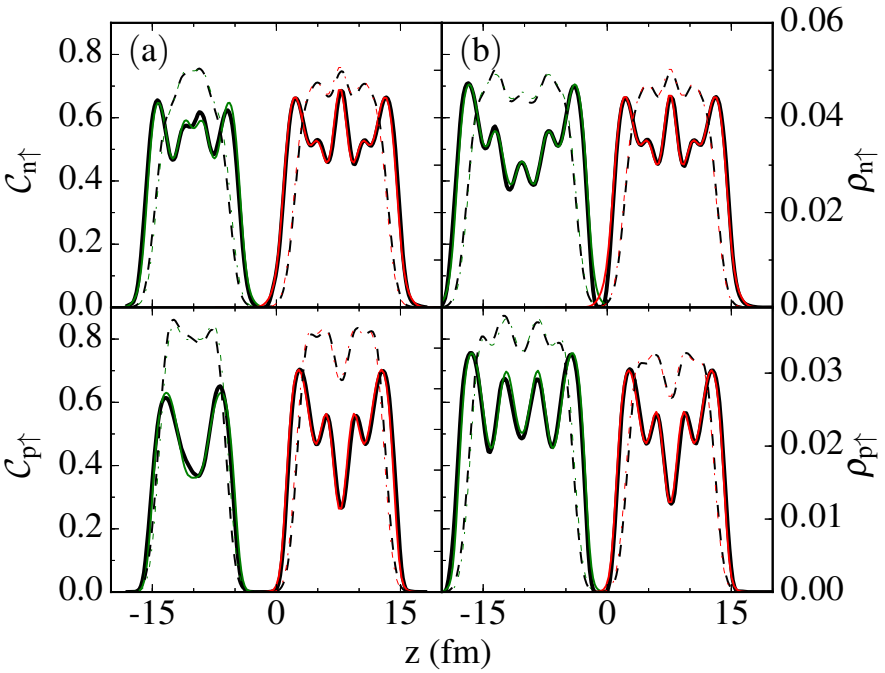


Figure 4.14: One-dimensional plots of $\mathcal{C}_{q\uparrow}$ (solid lines) and $\rho_{q\uparrow}$ (dashed lines) along the symmetry axis for the configurations $(a)$ and $(b)$ of Fig. 4.13. The black lines are results for the fragmented systems, while the green and red lines denote the results for fission fragments.

The outer turning line and scission line for $^{240}$Pu are shown in Fig. 4.13. The scission line corresponds to the deformation where spatial nucleon densities of the fission fragments are well separated. We first calculate the NLFs on this scission line. Corresponding one-dimensional plots of $\mathcal{C}_{q\sigma}$ and $\rho_{q\sigma}$ along the symmetry axis are shown in Fig. 4.14 for the two configurations as indicated in Fig. 4.13 by $(a)$ and $(b)$. Evidently, both the $\mathcal{C}_{q\sigma}$ and $\rho_{q\sigma}$ of the fragmented systems are indistinguishable from those of the corresponding fission fragments calculated separately. The oscillations in $\mathcal{C}_{q\sigma}$ uniquely determine the cluster structure of fission fragments that are absent in the scalar particle density obtained with $\rho_{q\sigma}$. Therefore, the NLF can be used as a more appropriate probe to identify the fission fragments.

The scenario changes appreciably at the outer turning line. We take configurations (1), (5) and (11) as examples to illustrate this. Only at lower values of $Q_{30}$ (configuration (1) of Fig. 4.13), where the outer turning line is very close to the scission point, a well defined

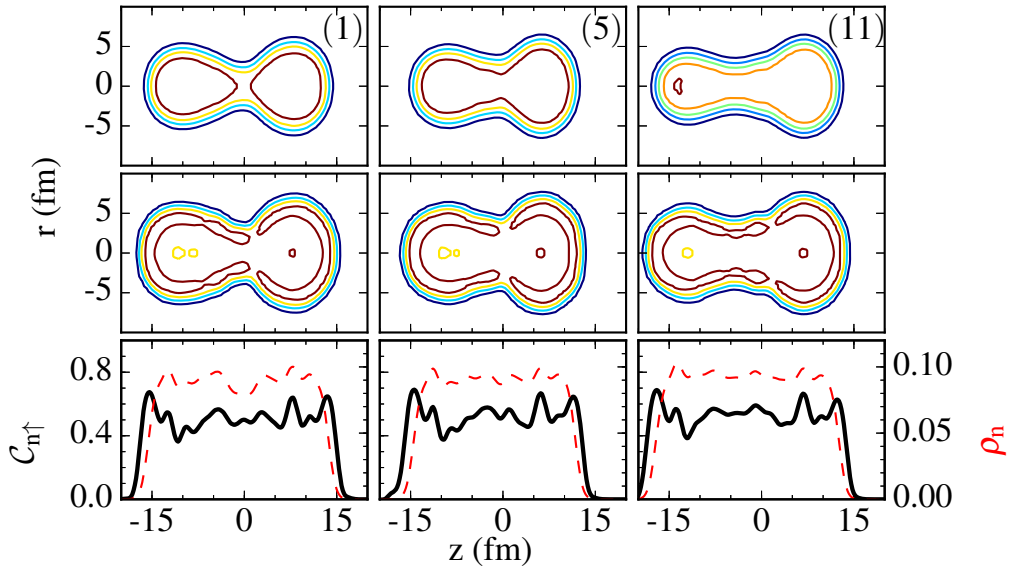


Figure 4.15: Contours of $\rho_n$ (top row) and $\mathcal{C}_{n\uparrow}$ of $^{240}$Pu (second row). The last row gives a comparison of one dimensional $\mathcal{C}_{n\uparrow}$ (thick solid lines) with $\rho_n$ (thick dashed lines). The three columns correspond to configurations (1), (5), and (11) of Fig. 4.13.

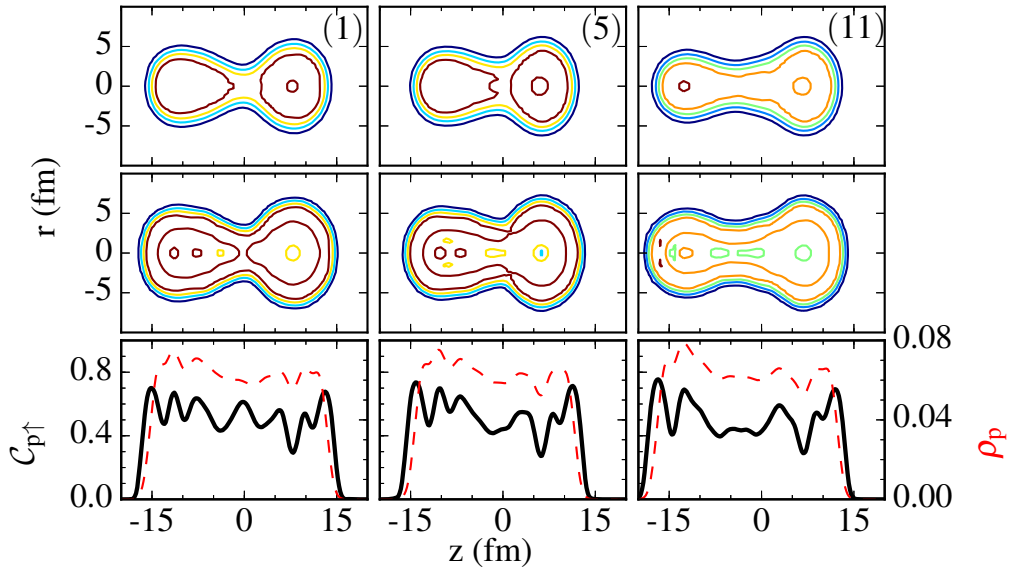


Figure 4.16: Same as Fig. 4.15, but for protons.

neck can be visualized from the nucleon density as shown in Fig. 4.15 and 4.16 for neutrons and protons, respectively. However, it is premature to predict the fission fragments with $\rho$ at configurations (5) and (11). Next, we compute $\mathcal{C}_{q\sigma}$ for all three configurations. As shown in Fig. 4.15 and 4.16, $\mathcal{C}_{q\sigma}$ calculated for each of the configurations shows remarkably

oscillating patterns and reveals more structure information as compared to the densities of the fissioning system.

In ongoing work, we will integrate over the outer parts of the density files for three configurations to obtain the very nascent fragments. By comparing the localizations calculated for the fragments with those for fissioning systems, the necks will be clearly defined.

## 4.5 Summary

In this work, we presented developments pertaining to the theoretical description of nucleonic clustering in light and heavy nuclei using the concept of nucleon localization. Following a schematic HO analysis, we carried out self-consistent DFT calculations for light $N = Z$ nuclei and heavy fissioning systems. We demonstrated that nucleon localization is a superb indicator of clustering in light and heavy nuclei; the characteristic patterns of NLFs can serve as fingerprints of the single-particle shell structure associated with cluster configurations.

In particular, the NLFs of $^{8}$Be,$^{12}$C, $^{16}$O, $^{20}$Ne and $^{24}$Mg can serve as excellent indicators of $\alpha$ clustering. Here, we found that the results of realistic HF calculations for NLFs are not significantly different from the results of the deformed HO model. This result suggests that the details of the EDF are perhaps not that important for the structure of cluster configurations in light nuclei, as the geometric properties of s.p. orbits robustly follow the HO description. While the characteristic oscillating patterns of the NLF magnify cluster structures in light nuclei, shell effects of nascent fragments in fissioning nuclei also leave a strong imprint on the localization. Our DFT analysis of fission evolution of $^{232}$Th, $^{264}$Fm and $^{240}$Pu demonstrates that the fragments are formed fairly early in the evolution, and the identification of these fragments before scission is very promising.

We also evaluated the nucleon localization level of $^{240}$Pu along the outer-turning line. For each considered configuration on the outer-turning line, a stochastic Langevin dynamics simulation will be performed to find the average paths to the scission line. This will allow us to identify fission fragments before scission.

# Chapter 5

# Conclusion and Outlook

This dissertation focused on several applications of nuclear DFT to collective states in atomic nuclei.

Two applications of nuclear DFT to nuclear rotation were presented. First, shape changes with rotation in triaxial $^{106,108}$Mo and $^{108,110,112}$Ru were studied as well as angular momentum alignment to rotational frequency. The computed transition quadrupole moments were compared to experiment.

Second, for $^{160}$Yb with triaxial deformation at high spins, nuclear DFT was employed to study strongly deformed bands through TAC calculations. The Kerman-Onishi condition was used to constrain the nucleus to stay in the PA system. The results showed that, at $\hbar\omega \approx 0.5$ MeV, the soft Routhian curve with respect to the tilted angle is indicative of the possible appearance of large-amplitude collective motion associated with the direction of angular momentum vector; with increasing rotational frequency, one of the two competing rotations (at tilted angle $0^\circ$ and $90^\circ$) became favored energetically and the other became an unphysical saddle point. To further understand the possible large-amplitude collective motion, methods beyond-mean-field, e.g. the generator coordinate method [18], must be employed.

As shown in the third project, spatial localization proved to be an excellent indicator of cluster structures and wave function correlations. A possible future research topic could be the evaluation of nucleon localization in nuclei under rotation, which is expected to show

configuration changes resulting from angular momentum alignment in the presence of broken time reversal symmetry and the current term in the NLF.

In our last project, we employed spatial localization to identify fission fragments before scission in $^{240}$Pu. The nucleon localizations at selected points on the outer-turning line and scission line were computed. The degree of localization in fission fragments along the fission pathway is closely related to the fragments' shell structures. Therefore, the effectiveness of identifying fission fragments with spatial localization is still under investigation.

In summary, this dissertation has shown that nuclear DFT can be successfully employed to study collective and single-particle effects in nuclei. However, the applications are not limited to those presented here. Other applications include the study of the zero-energy Nambu-Goldstone mode [163, 164], neutrinoless double-beta decay with beyond-mean-field DFT [165, 166] and nuclear pasta phases [30, 167] with time-dependent DFT, etc. The experience has given us the confidence to explore these problems.

# Chapter 6

# List of Publications and My Contributions

1. Yue Shi, **C. L. Zhang**, J. Dobaczewski, and W. Nazarewicz, "*Kerman-Onishi conditions in self-consistent tilted-axis-cranking mean-field calculations*", Phys. Rev. C **88**, 034311 (2013).

   • Performed PAC and TAC calculations to explain TSD bands in $^{160}$Yb.

   • Produced Fig. 4 in the paper.

2. **C. L. Zhang**, G. H. Bhat, W. Nazarewicz, J. A. Sheikh, and Yue Shi, "*Theoretical study of triaxial shapes of neutron-rich Mo and Ru nuclei*", Phys. Rev. C **92**, 034307 (2015).

   • Performed all the nuclear DFT calculations.

   • Produced the plots showing nuclear DFT results.

   • Wrote the first draft of the paper (except for Sec. II(B) and III(B)).

3. **C. L. Zhang**, B. Schuetrumpf, and W. Nazarewicz, "*Nucleon localization in light and heavy nuclei*", arXiv:1607.00422 (2016).

   • Implemented the axial harmonic oscillator model to calculate the nucleon localization.

   • Implemented nucleon localization extensions in HFBTHO and HFODD.

   • Performed all the calculations shown in this paper.

- Developed a Python code to produce all the plots shown in this paper.
- Wrote the first draft of the paper.

4. B. Schuetrumpf, **C. L. Zhang**, and W. Nazarewicz, "*Clustering and pasta phases in nuclear density functional theory*", arXiv:1607.01372 (2016).
   - Performed nucleon localization calculations for light and heavy nuclei with HFBTHO and HFODD.
   - Produced all the plots in Sec. 5.
5. Jhilam Sadhukhan, **C. L. Zhang**, W. Nazarewicz and Nicolas Schunk, "*Nucleon localization – a new tool to identify fission fragments*", in preparation.
   - Provided the nucleon localization module in HFODD to performed related calculations.
   - Produced the plots showing localization results.
6. R. Navarro Perez, N. Schunck, R. Lasseri, **C. L. Zhang** and J. Sarich "*Axially deformed solution of the Skyrme-Hartree-Fock-Bogolyubov equations using the transformed harmonic oscillator basis (III)* HFBTHO *v3.00: a new version of the program*", in preparation.
   - Implemented the nucleon localization module in HFBTHO.
   - Provided the tested input and output for localization calculations.

# APPENDICES

# Appendix A

# Hohenberg-Kohn theorems

**Hohenberg-Kohn theorem I:** There cannot be two external potentials, $U_{\text{ext},1}$ and $U_{\text{ext},2}$ ($U_{\text{ext},2} \neq U_{\text{ext},1}+const$) that give the same electron density. (i.e. given an external potential, the density is uniquely determined.)

**Proof I:** This can be proven with *reductio ad absurdum*.

With two external potentials, the Hamiltonians can be written as:

$$\hat{H}_1 = \hat{T} + \hat{V} + \hat{U}_{\text{ext},1}, \tag{A.1a}$$

$$\hat{H}_2 = \hat{T} + \hat{V} + \hat{U}_{\text{ext},2}. \tag{A.1b}$$

By diagonalizing the Hamiltonians, the ground eigenstates are given as $|\Psi_1\rangle$ and $|\Psi_2\rangle$, respectively, with ground eigenvalues $E_1$ and $E_2$.

Assuming that the ground state is non-degenerate and the same density, $\rho(\boldsymbol{r})$, is given by two external potentials, then,

$$\begin{aligned} E_1 \equiv \langle\Psi_1|\hat{H}_1|\Psi_1\rangle &< \langle\Psi_2|\hat{H}_1|\Psi_2\rangle \\ &= E_2 + \int d\boldsymbol{r}[U_{\text{ext},1}(\boldsymbol{r}) - U_{\text{ext},2}(\boldsymbol{r})]\rho(\boldsymbol{r}), \end{aligned} \tag{A.2}$$

$$\begin{aligned} E_2 \equiv \langle\Psi_2|\hat{H}_2|\Psi_2\rangle &< \langle\Psi_1|\hat{H}_2|\Psi_1\rangle \\ &= E_1 - \int d\boldsymbol{r}[U_{\text{ext},1}(\boldsymbol{r}) - U_{\text{ext},2}(\boldsymbol{r})]\rho(\boldsymbol{r}). \end{aligned} \tag{A.3}$$

Adding A.2 and A.3, we obtain

$$E_1 + E_2 < E_2 + E_1, \tag{A.4}$$

which is a contradiction. Thus, the theorem has been proven.

For the degenerate case, the theorem should be slightly modified: there cannot be two external potentials, $U_{\text{ext},1}$ and $U_{\text{ext},2}$ ($U_{\text{ext},2} \neq U_{\text{ext},1} + const$) that give the same **class of electron densities**. More details can be found in [168].

**Hohenberg-Kohn theorem II:** A universal functional for the energy $E[\rho(\boldsymbol{r})]$ can be defined in terms of the electron density, and is minimized when $\rho(\boldsymbol{r})$ is the ground state density.

**Proof II:** The energy of the interacting system can be written as:

$$E = \langle \Psi | \hat{H} | \Psi \rangle = \langle \Psi | \hat{T} + \hat{V} + \hat{U}_{\text{ext}} | \Psi \rangle \,. \tag{A.5}$$

Since the density is uniquely determined and we assume a non-degenerate ground state, the ground state wave function is also uniquely determined. Thus, the energy in terms of the wave function can be transformed into the functional of the density:

$$E[\rho(\boldsymbol{r})] = F[\rho(\boldsymbol{r})] + \int U_{\text{ext}}(\boldsymbol{r})\rho(\boldsymbol{r}) d\boldsymbol{r}. \tag{A.6}$$

The first term is a universal functional because the treatment of both the kinetic and potential energies is universal over all the interacting systems.

When $\rho(\boldsymbol{r})$ is ground state density, the ground state wave function is uniquely determined

as $|\Psi_{g.s.}\rangle$, then

$$E[\rho_{g.s.}] = \langle\Psi_{g.s.}|\hat{H}|\Psi_{g.s.}\rangle < \langle\Psi_2|\hat{H}|\Psi_2\rangle = E[\rho_2], \tag{A.7}$$

where $\rho_2$ is a different density from the ground state, and $|\Psi_2\rangle$ is the corresponding wave function. Therefore, the energy is minimized when $\rho$ is the exact ground state density.

# Appendix B

# Spatial Localization

The conditional probability of finding a nucleon at $\boldsymbol{r}_1$ when we know with certainty that another nucleon with the same spin and isospin is at $\boldsymbol{r}$ is [23]

$$R_{q\sigma}(\boldsymbol{r}, \boldsymbol{r}_1) = \rho_{q\sigma}(\boldsymbol{r}_1) - \frac{|\rho_{q\sigma\sigma}(\boldsymbol{r}, \boldsymbol{r}_1)|^2}{\rho_{q\sigma}(\boldsymbol{r})}. \tag{B.1}$$

Since we are only interested in the localization part of this probability, it is sufficient to consider the local short-range behavior of the conditional probability, which can be obtained by performing a spherical averaging over a shell of radius $\delta$ about the reference point $\boldsymbol{r}$. We perform the Taylor expansion in the coordinate $\boldsymbol{\delta}$ about the reference point $\boldsymbol{r}$ [169]:

$$R_{q\sigma}(\boldsymbol{r}, \boldsymbol{r} + \boldsymbol{\delta}) = e^{\boldsymbol{\delta}\cdot\nabla_1} R_{q\sigma}(\boldsymbol{r}, \boldsymbol{r}_1)|_{\boldsymbol{r}_1=\boldsymbol{r}}. \tag{B.2}$$

The spherical average of the Taylor expansion is given as

$$\begin{aligned} \langle e^{\boldsymbol{\delta}\cdot\nabla_1} \rangle =& \frac{1}{4\pi} \int e^{\boldsymbol{\delta}\cdot\nabla_1} d\Omega \\ =& \frac{\sinh(\delta\nabla_1)}{\delta\nabla_1} \\ =& 1 + \frac{1}{3!}\delta^2\nabla_1^2 + \frac{1}{5!}\delta^4\nabla_1^4 + \frac{1}{7!}\delta^6\nabla_1^6 + \cdots . \end{aligned} \tag{B.3}$$

Since

$$R_{q\sigma}(\boldsymbol{r}, \boldsymbol{r}_1)|_{\boldsymbol{r}_1=\boldsymbol{r}} = 0, \tag{B.4}$$

and

$$\nabla_1^2 \frac{|\rho_\sigma(\mathbf{r},\mathbf{r}_1)|^2}{\rho_\sigma(\mathbf{r})}|_{\mathbf{r}_1=\mathbf{r}} = \nabla^2\rho_\sigma(\mathbf{r}) - 2\tau_\sigma(\mathbf{r}) + \frac{1}{2}\frac{|\nabla\rho_\sigma(\mathbf{r})|^2}{\rho_\sigma(\mathbf{r})} + 2\boldsymbol{j}_\sigma^2(\mathbf{r}), \tag{B.5}$$

one can obtain

$$R_{q\sigma}(\boldsymbol{r},\delta) \approx \frac{1}{3}\left(\tau_{q\sigma} - \frac{1}{4}\frac{|\boldsymbol{\nabla}\rho_{q\sigma}|^2}{\rho_{q\sigma}} - \frac{\boldsymbol{j}_{q\sigma}^2}{\rho_{q\sigma}}\right)\delta^2 + \mathcal{O}(\delta^3). \tag{B.6}$$

If this conditional probability is small, it means that one nucleon with fixed spin and isospin is highly localized in the space. Therefore, the spatial localization has an inverse relation with the probability. To make the localization normalized and dimensionless, the spatial localization can be defined as

$$\mathcal{C}_{q\sigma}(\boldsymbol{r}) = \left[1 + \left(\frac{\tau_{q\sigma}\rho_{q\sigma} - \frac{1}{4}|\boldsymbol{\nabla}\rho_{q\sigma}|^2 - \boldsymbol{j}_{q\sigma}^2}{\rho_{q\sigma}\tau_{q\sigma}^{\mathrm{TF}}}\right)^2\right]^{-1}. \tag{B.7}$$

Proof of (B.5):

$$\begin{aligned}
&\nabla_1^2|\rho_\sigma(\mathbf{r},\mathbf{r}_1)|^2|_{\mathbf{r}_1=\mathbf{r}} \\
=&\nabla_1[\nabla_1\rho_\sigma(\mathbf{r},\mathbf{r}_1)\rho_\sigma^*(\mathbf{r},\mathbf{r}_1) + \rho_\sigma(\mathbf{r},\mathbf{r}_1)\nabla_1\rho_\sigma^*(\mathbf{r},\mathbf{r}_1)]|_{\mathbf{r}_1=\mathbf{r}} \\
=&[\nabla_1^2\rho_\sigma(\mathbf{r},\mathbf{r}_1)\rho_\sigma^*(\mathbf{r},\mathbf{r}_1) + 2\nabla_1\rho_\sigma(\mathbf{r},\mathbf{r}_1)\nabla_1\rho_\sigma^*(\mathbf{r},\mathbf{r}_1) + \rho_\sigma(\mathbf{r},\mathbf{r}_1)\nabla_1^2\rho_\sigma^*(\mathbf{r},\mathbf{r}_1)]|_{\mathbf{r}_1=\mathbf{r}},
\end{aligned} \tag{B.8}$$

where, 1st term + 3rd term:

$$
\begin{aligned}
&= [\nabla_1^2 \rho_\sigma(\mathbf{r}, \mathbf{r}_1)\rho_\sigma^*(\mathbf{r}) + \rho_\sigma(\mathbf{r})\nabla_1^2 \rho_\sigma^*(\mathbf{r}, \mathbf{r}_1)]|_{\mathbf{r}_1=\mathbf{r}} \\
&= \rho_\sigma(\mathbf{r})[\nabla_1^2 \rho_\sigma(\mathbf{r}, \mathbf{r}_1) + \nabla_1^2 \rho_\sigma^*(\mathbf{r}, \mathbf{r}_1)]|_{\mathbf{r}_1=\mathbf{r}} \\
&= \rho_\sigma(\mathbf{r})[\nabla_1^2 \rho_\sigma(\mathbf{r}, \mathbf{r}_1) + \nabla^2 \rho_\sigma(\mathbf{r}, \mathbf{r}_1)]|_{\mathbf{r}_1=\mathbf{r}} \\
&= \rho_\sigma(\mathbf{r})(\nabla_1^2 + \nabla^2)\rho_\sigma(\mathbf{r}, \mathbf{r}_1)|_{\mathbf{r}_1=\mathbf{r}} \\
&= \rho_\sigma(\mathbf{r})[(\nabla_1 + \nabla)^2 - 2\nabla_1 \cdot \nabla]\rho_\sigma(\mathbf{r}, \mathbf{r}_1)|_{\mathbf{r}_1=\mathbf{r}} \\
&= \rho_\sigma(\mathbf{r})[\nabla^2 \rho_\sigma(\mathbf{r}) - 2\tau_\sigma(\mathbf{r})]],
\end{aligned}
\tag{B.9}
$$

and, 2nd term:

$$
\begin{aligned}
&= 2\nabla_1 \rho_\sigma(\mathbf{r}, \mathbf{r}_1)\nabla_1 \rho_\sigma(\mathbf{r}_1, \mathbf{r})|_{\mathbf{r}_1=\mathbf{r}} \\
&= \frac{1}{2}[\nabla_1 \rho_\sigma(\mathbf{r}, \mathbf{r}_1) + \nabla_1 \rho_\sigma(\mathbf{r}_1, \mathbf{r})]^2 - \frac{1}{2}[\nabla_1 \rho_\sigma(\mathbf{r}, \mathbf{r}_1) - \nabla_1 \rho_\sigma(\mathbf{r}_1, \mathbf{r})]^2|_{\mathbf{r}_1=\mathbf{r}} \\
&= \frac{1}{2}[\nabla_1 \rho_\sigma(\mathbf{r}, \mathbf{r}_1) + \nabla \rho_\sigma(\mathbf{r}, \mathbf{r}_1)]^2 - \frac{1}{2}[\nabla_1 \rho_\sigma(\mathbf{r}, \mathbf{r}_1) - \nabla \rho_\sigma(\mathbf{r}, \mathbf{r}_1)]^2|_{\mathbf{r}_1=\mathbf{r}} \\
&= \frac{1}{2}[\nabla \rho_\sigma(\mathbf{r})]^2 - \frac{1}{2}[2i\boldsymbol{j}_\sigma(\mathbf{r})]^2 \\
&= \frac{1}{2}[\nabla \rho_\sigma(\mathbf{r})]^2 + 2\boldsymbol{j}_\sigma(\mathbf{r})^2,
\end{aligned}
\tag{B.10}
$$

then,

$$
\nabla_1^2 \frac{|\rho_\sigma(\mathbf{r}, \mathbf{r}_1)|^2}{\rho_\sigma(\mathbf{r})}|_{\mathbf{r}_1=\mathbf{r}} = \nabla^2 \rho_\sigma(\mathbf{r}) - 2\tau_\sigma(\mathbf{r}) + \frac{1}{2}\frac{|\nabla \rho_\sigma(\mathbf{r})|^2}{\rho_\sigma(\mathbf{r})} + 2\boldsymbol{j}_\sigma^2(\mathbf{r}). \tag{B.11}
$$

# BIBLIOGRAPHY

# BIBLIOGRAPHY


[1] J. Dobaczewski and P. Olbratowski, "Solution of the skyrme–hartree–fock–bogolyubov equations in the cartesian deformed harmonic-oscillator basis.(iv) HFODD (v2. 08i): a new version of the program," *Comput. Phys. Commun.*, vol. 158, no. 3, pp. 158–191, 2004.

[2] H. Hua *et al.*, "Triaxiality and the aligned $h_{112}$ neutron orbitals in neutron-rich Zr and Mo isotopes," *Phys. Rev. C*, vol. 69, p. 014317, Jan 2004.

[3] Q. H. Lu *et al.*, "Structure of $^{108,110,112}$Ru: Identical bands in $^{108,110}$Ru," *Phys. Rev. C*, vol. 52, pp. 1348–1354, Sep 1995.

[4] C. Y. Wu, H. Hua, D. Cline, A. B. Hayes, R. Teng, D. Riley, R. M. Clark, P. Fallon, A. Goergen, A. O. Macchiavelli, and K. Vetter, "Evidence for possible shape transitions in neutron-rich Ru isotopes: Spectroscopy of $^{109,110,111,112}$Ru," *Phys. Rev. C*, vol. 73, p. 034312, 2006.

[5] S. Raman, C. Malarkey, W. Milner, C. N. Jr., and P. Stelson, "Transition probability, b(e2)↑, from the ground to the first-excited 2+ state of even-even nuclides," *At. Data Nucl. Data Tables*, vol. 36, no. 1, pp. 1 – 96, 1987.

[6] J. Snyder *et al.*, "High-spin transition quadrupole moments in neutron-rich Mo and Ru nuclei: Testing $\gamma$ softness?," *Phys. Lett. B*, vol. 723, no. 1, pp. 61–65, 2013.

[7] J. D. McDonnell, W. Nazarewicz, and J. A. Sheikh, "Third minima in thorium and uranium isotopes in a self-consistent theory," *Phys. Rev. C*, vol. 87, p. 054327, May 2013.

[8] J. Sadhukhan, W. Nazarewicz, and N. Schunck, "Microscopic modeling of mass and charge distributions in the spontaneous fission of $^{240}$Pu," *Phys. Rev. C*, vol. 93, no. 1, p. 011304, 2016.

[9] J. Carlson, "Green's function monte carlo study of light nuclei," *Phys. Rev. C*, vol. 36, no. 5, p. 2026, 1987.

[10] S. C. Pieper and R. B. Wiringa, "Quantum monte carlo calculations of light nuclei," *arXiv preprint nucl-th/0103005*, 2001.

[11] P. Navrátil, J. Vary, and B. R. Barrett, "Large-basis ab initio no-core shell model and its application to $^{12}$C," *Phys. Rev. C*, vol. 62, no. 5, p. 054311, 2000.

[12] P. Navrátil, S. Quaglioni, I. Stetcu, and B. R. Barrett, "Recent developments in no-core shell-model calculations," *J. Phys. G: Nucl. Part. Phys.*, vol. 36, no. 8, p. 083101, 2009.

[13] B. R. Barrett, P. Navrátil, and J. P. Vary, "Ab initio no core shell model," *Prog. Part. Nucl. Phys.*, vol. 69, pp. 131–181, 2013.

[14] N. Michel, W. Nazarewicz, M. Płoszajczak, and J. Okołowicz, "Gamow shell model description of weakly bound nuclei and unbound nuclear states," *Phys. Rev. C*, vol. 67, no. 5, p. 054311, 2003.

[15] G. Hagen, M. Hjorth-Jensen, and N. Michel, "Gamow shell model and realistic nucleon-nucleon interactions," *Phys. Rev. C*, vol. 73, no. 6, p. 064307, 2006.

[16] J. Dobaczewski, "Current developments in nuclear density functional methods," in *JPCS*, vol. 312, p. 092002, IOP Publishing, 2011.

[17] M. Bender, P.-H. Heenen, and P.-G. Reinhard, "Self-consistent mean-field models for nuclear structure," *Rev. Mod. Phys.*, vol. 75, no. 1, p. 121, 2003.

[18] P. Ring and P. Schuck, *The Nuclear Many-Body Problem.* 1980.

[19] S. Frauendorf, "Spontaneous symmetry breaking in rotating nuclei," *Rev. Mod. Phys.*, vol. 73, pp. 463–514, Jun 2001.

[20] I. Hamamoto, "Band crossing in the cranking model," *Nucl. Phys. A*, vol. 271, no. 1, pp. 15–28, 1976.

[21] S. Ćwiok, W. Nazarewicz, J. Dudek, J. Skalski, and Z. Szymański, "Microscopic analysis of the double backbending in the nucleus $^{160}$Yb," *Nucl. Phys. A*, vol. 333, no. 1, p. 139, 1980.

[22] A. D. Becke and K. E. Edgecombe, "A simple measure of electron localization in atomic and molecular systems," *J. Phys. Chem.*, vol. 92, no. 9, p. 5397, 1990.

[23] P.-G. Reinhard, J. A. Maruhn, A. S. Umar, and V. E. Oberacker, "Localization in light nuclei," *Phys. Rev. C*, vol. 83, p. 034312, mar 2011.

[24] C. L. Zhang, B. Schuetrumpf, and W. Nazarewicz, "Nucleon localization in light and heavy nuclei," *arXiv preprint arXiv:1607.00422*, 2016.

[25] S. Ćwiok, P.-H. Heenen, and W. Nazarewicz, "Shape coexistence and triaxiality in the superheavy nuclei," *Nature*, vol. 433, no. 7027, pp. 705–709, 2005.

[26] J. Erler, N. Birge, M. Kortelainen, W. Nazarewicz, E. Olsen, A. M. Perhac, and M. Stoitsov, "The limits of the nuclear landscape," *Nature*, vol. 486, p. 509, 2012.

[27] E. Olsen, M. Pfützner, N. Birge, M. Brown, W. Nazarewicz, and A. Perhac, "Landscape of two-proton radioactivity," *Phys. Rev. Lett.*, vol. 110, no. 22, p. 222501, 2013.

[28] W. Nazarewicz, "Rotational properties of neutron drip-line nuclei," tech. rep., Oak Ridge National Lab., TN (US), 2001.

[29] C. L. Zhang, G. H. Bhat, W. Nazarewicz, J. Sheikh, and Y. Shi, "Theoretical study of triaxial shapes of neutron-rich Mo and Ru nuclei," *Phys. Rev. C*, vol. 92, no. 3, p. 034307, 2015.

[30] T. Maruyama, T. Tatsumi, D. N. Voskresensky, T. Tanigawa, and S. Chiba, "Nuclear "pasta" structures and the charge screening effect," *Phys. Rev. C*, vol. 72, no. 1, p. 015802, 2005.

[31] B. Schuetrumpf, C. Zhang, and W. Nazarewicz, "Clustering and pasta phases in nuclear density functional theory," *arXiv preprint arXiv:1607.01372*, 2016.

[32] Z. Szymański, *Fast nuclear rotation*. Oxford University Press, 1983.

[33] J. Skalski, S. Mizutori, and W. Nazarewicz, "Equilibrium shapes and high–spin properties of the neutron-rich A $\approx$ 100 nuclei," *Nucl. Phys. A*, vol. 617, no. 3, pp. 282 – 315, 1997.

[34] S. G. Frauendorf and J. A. Sheikh, "Cranked shell model and isospin symmetry near n= z," *Nucl. Phys. A*, vol. 645, no. 4, pp. 509–535, 1999.

[35] F. Xu, P. Walker, and R. Wyss, "Oblate stability of a 110 nuclei near the r-process path," *Phys. Rev. C*, vol. 65, no. 2, p. 021303, 2002.

[36] R. Rodríguez-Guzmán, P. Sarriguren, L. Robledo, and S. Perez-Martin, "Charge radii and structural evolution in Sr, Zr, and Mo isotopes," *Phys. Lett. B*, vol. 691, no. 4, pp. 202 – 207, 2010.

[37] K. Nomura, N. Shimizu, and T. Otsuka, "Formulating the interacting boson model by mean-field methods," *Phys. Rev. C*, vol. 81, p. 044307, Apr 2010.

[38] I. Bentley and S. Frauendorf, "Microscopic calculation of interacting boson model parameters by potential-energy surface mapping," *Phys. Rev. C*, vol. 83, p. 064322, Jun 2011.

[39] C. Beck, *Clusters in Nuclei*, vol. 1. Springer-Verlag Berlin Heidelberg, 2010.

[40] C. Beck, *Clusters in Nuclei*, vol. 2. Springer-Verlag Berlin Heidelberg, 2012.

[41] C. Beck, *Clusters in Nuclei*, vol. 3. Springer International Publishing, 2014.

[42] W. von Oertzen, M. Freer, and Y. Kanada-En′yo, "Nuclear clusters and nuclear molecules," *Phys. Rep.*, vol. 432, no. 2, pp. 43 – 113, 2006.

[43] D. S. Delion, *Theory of Particle and Cluster Emission*, vol. 829 of *Lecture Notes in Physics*. Springer-Verlag Berlin Heidelberg, 2010.

[44] L. R. Hafstad and E. Teller, "The alpha-particle model of the nucleus," *Phys. Rev.*, vol. 54, p. 681, Nov 1938.

[45] H. J. Rose and G. A. Jones, "A new kind of natural radioactivity," *Nature*, vol. 307, pp. 245–247, jan 1984.

[46] D. V. Aleksandrov, A. F. Belyatskiĭ, Y. A. Glukhov, E. Y. Nikol'Skiĭ, B. G. Novatskiĭ, A. A. Ogloblin, and D. N. Stepanov, "Observation of the spontaneous emission of $^{14}$C nuclei from $^{223}$Ra," *ZhETF Pisma Redaktsiiu*, vol. 40, p. 152, Aug. 1984.

[47] S. Bjørnholm and J. E. Lynn, "The double-humped fission barrier," *Rev. Mod. Phys.*, vol. 52, pp. 725–931, Oct 1980.

[48] G. Röpke, A. Grigo, K. Sumiyoshi, and H. Shen, *Clusters and condendates in the nuclear matter equation of state*, p. 73. Dordrecht: Springer Netherlands, 2006.

[49] M. Girod and P. Schuck, "$\alpha$-particle clustering from expanding self-conjugate nuclei within the hartree–fock–bogoliubov approach," *Phys. Rev. Lett.*, vol. 111, p. 132503, Sep 2013.

[50] J.-P. Ebran, E. Khan, T. Nikšić, and D. Vretenar, "Cluster–liquid transition in finite, saturated fermionic systems," *Phys. Rev. C*, vol. 89, p. 031303, Mar 2014.

[51] D. Brink and J. Castro, "Alpha clustering effects in nuclear matter," *Nucl. Phys. A*, vol. 216, p. 109, 1973.

[52] J. Okołowicz, M. Płoszajczak, and W. Nazarewicz, "On the origin of nuclear clustering," *Prog. Theor. Phys. Suppl.*, vol. 196, p. 230, 2012.

[53] J. Okołowicz, W. Nazarewicz, and M. Płoszajczak, "Toward understanding the microscopic origin of nuclear clustering," *Fortschr. Phys.*, vol. 61, pp. 66–79, 2013.

[54] K. Ikeda, N. Takigawa, and H. Horiuchi, "The systematic structure-change into the molecule-like structures in the self-conjugate 4n nuclei," *Prog. Theor. Phys. Suppl.*, vol. E68, p. 464, 1968.

[55] R. G. Lovas, Z. Dombrádi, G. G. Kiss, A. T. Kruppa, and G. Lévai, eds., *10th International Conference on Clustering Aspects of Nuclear Structure and Dynamics*, vol. 436, 2013.

[56] T. Yoshida, N. Shimizu, T. Abe, and T. Otsuka, "Cluster structure in monte carlo shell model," *J. Phys. Conf. Ser.*, vol. 454, no. 1, p. 012050, 2013.

[57] E. Epelbaum, H. Krebs, T. A. Lähde, D. Lee, and U.-G. Meißner, "Structure and rotations of the hoyle state," *Phys. Rev. Lett.*, vol. 109, p. 252501, Dec 2012.

[58] E. Epelbaum, H. Krebs, T. A. Lähde, D. Lee, U.-G. Meißner, and G. Rupak, "*Ab Initio* calculation of the spectrum and structure of $^{16}$O," *Phys. Rev. Lett.*, vol. 112, p. 102501, Mar 2014.

[59] S. Elhatisari, D. Lee, G. Rupak, E. Epelbaum, H. Krebs, T. A. Lähde, T. Luu, and U.-G. Meißner, "Ab initio alpha–alpha scattering," *Nature*, vol. 528, p. 111, 2015.

[60] J. Carlson, S. Gandolfi, F. Pederiva, S. C. Pieper, R. Schiavilla, K. E. Schmidt, and R. B. Wiringa, "Quantum monte carlo methods for nuclear physics," *Rev. Mod. Phys.*, vol. 87, pp. 1067–1118, Sep 2015.

[61] G. Leander and S. Larsson, "Potential-energy surfaces for the doubly even N = Z nuclei," *Nucl. Phys. A*, vol. 239, p. 93, 1975.

[62] H. Flocard, P. H. Heenen, S. J. Krieger, and M. S. Weiss, "Configuration space, cranked hartree–fock calculations for the nuclei $^{16}$O, $^{24}$Mg and $^{32}$S," *Prog. Theor. Phys.*, vol. 72, no. 5, pp. 1000–1016, 1984.

[63] S. Marsh and W. Rae, "The structure of $^{24}$Mg using the cranked cluster model," *Phys. Lett. B*, vol. 180, no. 3, pp. 185 – 190, 1986.

[64] M. Freer, R. Betts, and A. Wuosmaa, "Relationship between the deformed harmonic oscillator and clustering in light nuclei," *Nucl. Phys. A*, vol. 587, no. 1, pp. 36 – 54, 1995.

[65] J. Maruhn, N. Loebl, N. Itagaki, and M. Kimura, "Linear-chain structure of three $\alpha$-clusters in $^{16}$C and $^{20}$C," *Nucl. Phys. A*, vol. 833, no. 1, pp. 1–17, 2010.

[66] T. Ichikawa, J. A. Maruhn, N. Itagaki, and S. Ohkubo, "Linear chain structure of four-$\alpha$ clusters in $^{16}$O," *Phys. Rev. Lett.*, vol. 107, p. 112501, 2011.

[67] J.-P. Ebran, E. Khan, T. Nikšić, and D. Vretenar, "How atomic nuclei cluster," *Nature*, vol. 487, no. 7407, pp. 341–344, 2012.

[68] J.-P. Ebran, E. Khan, T. Nikšić, and D. Vretenar, "Density functional theory studies of cluster states in nuclei," *Phys. Rev. C*, vol. 90, no. 5, p. 054329, 2014.

[69] K. T. Hecht, "Relation between cluster and shell-model wave functions," *Phys. Rev. C*, vol. 16, p. 2401, 1977.

[70] W. Nazarewicz and J. Dobaczewski, "Dynamical symmetries, multiclustering, and octupole susceptibility in superdeformed and hyperdeformed nuclei," *Phys. Rev. Lett.*, vol. 68, no. 2, p. 154, 1992.

[71] P. Hohenberg and W. Kohn, "Inhomogeneous electron gas," *Phys. Rev.*, vol. 136, no. 3B, p. B864, 1964.

[72] T. Skyrme, "Cvii. the nuclear surface," *Philos. Mag.*, vol. 1, no. 11, pp. 1043–1054, 1956.

[73] T. Skyrme, "The effective nuclear potential," *Nucl. Phys.*, vol. 9, no. 4, pp. 615–634, 1959.

[74] D. Gogny, "Proceedings of the international conference on nuclear self-consistent fields, trieste, 1975," 1975.

[75] J. Meng, "Relativistic continuum hartree-bogoliubov theory with both zero range and finite range gogny force and their application," *Nucl. Phys. A*, vol. 635, no. 1, pp. 3–42, 1998.

[76] F. Chappert, N. Pillet, M. Girod, and J.-F. Berger, "Gogny force with a finite-range density dependence," *Phys. Rev. C*, vol. 91, no. 3, p. 034312, 2015.

[77] M. Grasso, D. Lacroix, and U. van Kolck, "From effective field theories to effective density functionals in and beyond the mean field," *Phys. Scripta*, vol. 91, no. 6, p. 063005, 2016.

[78] M. Kortelainen, T. Lesinski, J. Moré, W. Nazarewicz, J. Sarich, N. Schunck, M. V. Stoitsov, and S. Wild, "Nuclear energy density optimization," *Phys. Rev. C*, vol. 82, p. 024313, Aug 2010.

[79] Y. Engel, D. Brink, K. Goeke, S. Krieger, and D. Vautherin, "Time-dependent hartree-fock theory with skyrme's interaction," *Nucl. Phys. A*, vol. 249, no. 2, pp. 215–238, 1975.

[80] J. Dobaczewski and J. Dudek, "Solution of the skyrme–hartree–fock equations in the cartesian deformed harmonic oscillator basis i. the method," *Comput. Phys. Commun.*, vol. 102, no. 1, pp. 166–182, 1997.

[81] M. Beiner, H. Flocard, N. Van Giai, and P. Quentin, "Nuclear ground-state properties and self-consistent calculations with the skyrme interaction:(i). spherical description," *Nucl. Phys. A*, vol. 238, no. 1, pp. 29–69, 1975.

[82] D. Vautherin and D. t. Brink, "Hartree–fock calculations with skyrme's interaction. i. spherical nuclei," *Phys. Rev. C*, vol. 5, no. 3, p. 626, 1972.

[83] J. Terasaki, H. Flocard, P.-H. Heenen, and P. Bonche, "Deformation of nuclei close to the two-neutron drip line in mg region," *Acta Phys Hung New Ser Heavy Ion Phys*, vol. 6, no. 1-4, pp. 201–204, 1997.

[84] J. C. Slater, "A simplification of the hartree–fock method," *Phys. Rev.*, vol. 81, no. 3, p. 385, 1951.

[85] C. Titin-Schnaider and P. Quentin, "Coulomb exchange contribution in nuclear hartree–fock calculations," *Phys. Lett. B*, vol. 49, no. 5, pp. 397–400, 1974.

[86] J. Bartel, P. Quentin, M. Brack, C. Guet, and H.-B. Håkansson, "Towards a better parametrisation of skyrme-like effective forces: A critical study of the skm force," *Nucl. Phys. A*, vol. 386, no. 1, pp. 79–100, 1982.

[87] J. Dobaczewski, H. Flocard, and J. Treiner, "Hartree–fock–bogolyubov description of nuclei near the neutron-drip line," *Nucl. Phys. A*, vol. 422, no. 1, pp. 103–139, 1984.

[88] E. Chabanat, P. Bonche, P. Haensel, J. Meyer, and R. Schaeffer, "A skyrme parametrization from subnuclear to neutron star densities part ii. nuclei far from stabilities," *Nucl. Phys. A*, vol. 635, no. 1, pp. 231–256, 1998.

[89] P. Klüpfel, P.-G. Reinhard, T. Bürvenich, and J. Maruhn, "Variations on a theme by skyrme: A systematic study of adjustments of model parameters," *Phys. Rev. C*, vol. 79, no. 3, p. 034310, 2009.

[90] M. Kortelainen, J. McDonnell, W. Nazarewicz, P.-G. Reinhard, J. Sarich, N. Schunck, M. Stoitsov, and S. Wild, "Nuclear energy density optimization: Large deformations," *Phys. Rev. C*, vol. 85, no. 2, p. 024304, 2012.

[91] N. Schunck, J. D. McDonnell, J. Sarich, S. M. Wild, and D. Higdon, "Error analysis in nuclear density functional theory," *J. Phys. G: Nucl. Part. Phys.*, vol. 42, no. 3, p. 034024, 2015.

[92] M. Kortelainen *et al.*, "Nuclear energy density optimization: Shell structure," *Phys. Rev. C*, vol. 89, no. 5, p. 054314, 2014.

[93] W. Kohn and L. J. Sham, "Self-consistent equations including exchange and correlation effects," *Phys. Rev.*, vol. 140, no. 4A, p. A1133, 1965.

[94] M. Stoitsov, J. Dobaczewski, W. Nazarewicz, and P. Ring, "Axially deformed solution of the skyrme-hartree-fock-bogolyubov equations using the transformed harmonic oscillator basis. the program HFBTHO (v1. 66p)," *Comput. Phys. Commun.*, vol. 167, no. 1, pp. 43–63, 2005.

[95] J. Dobaczewski and J. Dudek, "Time-odd components in the mean field of rotating superdeformed nuclei," *Phys. Rev. C*, vol. 52, no. 4, p. 1827, 1995.

[96] M. Stoitsov, N. Schunck, M. Kortelainen, N. Michel, H. Nam, E. Olsen, J. Sarich, and S. Wild, "Axially deformed solution of the skyrme-hartree-fock-bogoliubov equations using the transformed harmonic oscillator basis (ii) HFBTHO v2. 00d: A new version of the program," *Comput. Phys. Commun.*, vol. 184, no. 6, pp. 1592–1604, 2013.

[97] I. Z. Petkov and M. Stoitsov, "Local scale transformation method for the ground state of many-particle systems," *Theor. Math. Phys.*, vol. 55, no. 3, pp. 584–592, 1983.

[98] I. Z. Petkov and M. Stoitsov, *Nuclear density functional theory*, vol. 14. Oxford University Press, USA, 1991.

[99] J. Dobaczewski and J. Dudek, "Solution of the skyrme–hartree–fock equations in the cartesian deformed harmonic oscillator basis ii. the program HFODD," *Comput. Phys. Commun.*, vol. 102, no. 1, pp. 183–209, 1997.

[100] J. Dobaczewski and J. Dudek, "Solution of the skyrme–hartree–fock equations in the cartesian deformed harmonic-oscillator basis. (iii) HFODD (v1.75r): a new version of the program," *Comput. Phys. Commun.*, vol. 131, no. 1-2, pp. 164 – 186, 2000.

[101] J. Dobaczewski and P. Olbratowski, "Solution of the skyrme–hartree–fock–bogolyubov equations in the cartesian deformed harmonic-oscillator basis.(v) HFODD (v2. 08k)," *Comput. Phys. Commun.*, vol. 167, no. 3, pp. 214–216, 2005.

[102] J. Dobaczewski *et al.*, "Solution of the skyrme–hartree–fock–bogolyubov equations in the cartesian deformed harmonic-oscillator basis.:(vi) HFODD (v2. 40h): A new version of the program," *Comput. Phys. Commun.*, vol. 180, no. 11, pp. 2361–2391, 2009.

[103] N. Schunck, J. Dobaczewski, J. McDonnell, W. Satuła, J. Sheikh, A. Staszczak, M. Stoitsov, and P. Toivanen, "Solution of the skyrme–hartree–fock–bogolyubov equations in the cartesian deformed harmonic-oscillator basis.:(vii) HFODD (v2. 49t): A new version of the program," *Comput. Phys. Commun.*, vol. 183, no. 1, pp. 166–192, 2012.

[104] Y. Shi, C. L. Zhang, J. Dobaczewski, and W. Nazarewicz, "Kerman-onishi conditions in self-consistent tilted-axis-cranking mean-field calculations," *Phys. Rev. C*, vol. 88, p. 034311, Sep 2013.

[105] K. Heyde and J. L. Wood, "Shape coexistence in atomic nuclei," *Rev. Mod. Phys.*, vol. 83, no. 4, p. 1467, 2011.

[106] E. Cheifetz, R. Jared, S. Thompson, and J. Wilhelmy, "Experimental information concerning deformation of neutron rich nuclei in the A $\sim$ 100 region," *Phys. Rev. Lett.*, vol. 25, no. 1, p. 38, 1970.

[107] M. Hotchkins, J. Durell, J. Fitzgerald, A. Mowbray, W. Phillips, I. Ahmad, M. Carpenter, R. Janssens, T. Khoo, E. Moore, L. Morss, P. Benet, and D. Ye, "Rotational bands in the mass 100 region," *Nucl. Phys. A*, vol. 530, no. 1, pp. 111 – 134, 1991.

[108] J. Stachel, N. Kaffrell, E. Grosse, H. Emling, H. Folger, R. Kulessa, and D. Schwalm, "Triaxiality and its dynamics in 104ru investigated by multiple coulomb excitation," *Nucl. Phys. A*, vol. 383, no. 3, pp. 429 – 467, 1982.

[109] Äystö, P. Jauho, Z. Janas, A. Jokinen, J. Parmonen, H. Penttilä, P. Taskinen, R. Béraud, R. Duffait, A. Emsallem, J. Meyer, M. Meyer, N. Redon, M. Leino, K. Eskola, and P. Dendooven, "Collective structure of the neutron–rich nuclei, $^{110}$Ru and $^{112}$Ru," *Nucl. Phys. A*, vol. 515, no. 3, pp. 365 – 380, 1990.

[110] J. Shannon *et al.*, "The role of triaxiality in the ground states of even-even neutron-rich Ru isotopes," *Phys. Lett. B*, vol. 336, no. 2, pp. 136 – 140, 1994.

[111] J. H. Hamilton *et al.*, "New insights into the collective band structures of nuclei with A =100–112," *AIP Conf. Proc.*, vol. 1175, pp. 166–173, 2009.

[112] J. H. Hamilton *et al.*, "Super deformation to maximum triaxiality in ; superdeformation, chiral bands and wobbling motion," *Nucl. Phys. A*, vol. 834, pp. 28c–31c, 2010.

[113] W. Urban, T. Rzaca-Urban, J. Durell, W. Phillips, A. Smith, B. Varley, I. Ahmad, and N. Schulz, "First observation of excited states in the $^{110}$Mo nucleus," *Eur. Phys. J. A*, vol. 20, no. 3, pp. 381–384, 2004.

[114] H. Watanabe, K. Yamaguchi, A. Odahara, T. Sumikama, S. Nishimura, K. Yoshinaga, Z. Li, Y. Miyashita, and K. Sato, "Development of axial asymmetry in the neutron-rich nucleus $^{110}$Mo," *Phys. Lett. B*, vol. 704, no. 4, pp. 270 – 275, 2011.

[115] J. Srebrny, T. Czosnyka, and C. Droste, "Experimental and theoretical investigations of quadrupole collective degrees of freedom in $^{104}$Ru," *Nucl. Phys. A*, vol. 766, no. 0, pp. 25 – 51, 2006.

[116] P. Möller, R. Bengtsson, B. G. Carlsson, P. Olivius, and T. Ichikawa, "Global calculations of ground-state axial shape asymmetry of nuclei," *Phys. Rev. Lett.*, vol. 97, p. 162502, Oct 2006.

[117] Möller, R. Bengtsson, B. Carlsson, P. Olivius, T. Ichikawa, H. Sagawa, and A. Iwamoto, "Axial and reflection asymmetry of the nuclear ground state," *At. Data Nucl. Data Tab.*, vol. 94, no. 5, pp. 758 – 780, 2008.

[118] S. Frauendorf and J. Meng, "Tilted rotation of triaxial nuclei," *Nucl. Phys. A*, vol. 617, no. 2, pp. 131–147, 1997.

[119] D. Inglis, "Particle derivation of nuclear rotation properties associated with a surface wave," *Phys. Rev.*, vol. 96, no. 4, p. 1059, 1954.

[120] A. Kerman and O. Naoki, "Nuclear rotations studied by the time-dependent variational method," *Nucl. Phys. A*, vol. 361, no. 1, pp. 179–191, 1981.

[121] Y. Shi, J. Dobaczewski, S. Frauendorf, W. Nazarewicz, J. C. Pei, F. R. Xu, and N. Nikolov, "Self-consistent tilted-axis-cranking study of triaxial strongly deformed bands in $^{158}$Er at ultrahigh spin," *Phys. Rev. Lett.*, vol. 108, p. 092501, Feb 2012.

[122] P. Ring and P. Schuck, *The nuclear many-body problem*. Springer Science & Business Media, 2004.

[123] J. Dobaczewski, J. Dudek, S. Rohoziński, and T. Werner, "Point symmetries in the hartree–fock approach. i. densities, shapes, and currents," *Phys. Rev. C*, vol. 62, no. 1, p. 014310, 2000.

[124] A. Faessler, L. Lin, and F. Wittmann, "The coriolis anti pairing effect and angular momentum projection in rare earth nuclei," *Phys. Lett. B*, vol. 44, no. 2, pp. 127–130, 1973.

[125] A. Staszczak, M. Stoitsov, A. Baran, and W. Nazarewicz, "Augmented lagrangian method for constrained nuclear density functional theory," *Eur. Phys. J. A*, vol. 46, p. 85, 2010.

[126] D. Galeriu, D. Bucurescu, and M. Ivascu, "Nuclear deformations in the A $\approx$ 80-100 region," *J. Phys. G: Nucl. Part. Phys.*, vol. 12, no. 4, p. 329, 1986.

[127] J. Q. Faisal, H. Hua, X. Q. Li, Y. Shi, F. R. Xu, H. L. Liu, Y. L. Ye, and D. X. Jiang, "Shape evolutions in the neutron-rich Ru isotopes," *Phys. Rev. C*, vol. 82, p. 014321, Jul 2010.

[128] A. Axelsson, R. Bengtsson, and J. Nyberg, "An investigation of pairing correlations in diabatic configurations at high spin and large deformation: applications to the description of SD bands in $^{143}$Eu," *Nucl. Phys. A*, vol. 708, p. 245, 2002.

[129] W. Nazarewicz, J. Dudek, R. Bengtsson, T. Bengtsson, and I. Ragnarsson, "Microscopic study of the high-spin behaviour in selected A $\simeq$ 80 nuclei," *Nucl. Phys. A*, vol. 435, no. 2, pp. 397 – 447, 1985.

[130] J. Dudek, W. Nazarewicz, and N. Rowley, "Shape coexistence effects and superdeformation in $^{84}$Zr," *Phys. Rev. C*, vol. 35, pp. 1489–1501, Apr 1987.

[131] W. Satuła, J. Dobaczewski, J. Dudek, and W. Nazarewicz, "Additivity of quadrupole moments in superdeformed bands: Single-particle motion at extreme conditions," *Phys. Rev. Lett.*, vol. 77, pp. 5182–5185, Dec 1996.

[132] M. Matev, A. V. Afanasjev, J. Dobaczewski, G. A. Lalazissis, and W. Nazarewicz, "Additivity of effective quadrupole moments and angular momentum alignments in A $\sim$ 130 nuclei," *Phys. Rev. C*, vol. 76, p. 034304, Sep 2007.

[133] A. Aguilar *et al.*, "New shape minimum in $^{160}$Yb: Evidence for a triaxial, strongly deformed band," *Phys. Rev. C*, vol. 77, no. 2, p. 021302, 2008.

[134] A. V. Afanasjev, Y. Shi, and W. Nazarewicz, "Description of $^{158}$Er at ultrahigh spin in nuclear density functional theory," *Phys. Rev. C*, vol. 86, p. 031304, Sep 2012.

[135] A. Savin, R. Nesper, S. Wengert, and T. F. Fässler, "Elf: The electron localization function," *Angew. Chem. Int. Ed. Engl.*, vol. 36, no. 17, pp. 1808–1832, 1997.

[136] A. Scemama, P. Chaquin, and M. Caffarel, "Electron pair localization function: A practical tool to visualize electron localization in molecules from quantum monte carlo data," *J. Chem. Phys.*, vol. 121, no. 4, pp. 1725–1735, 2004.

[137] M. Kohout, "A measure of electron localizability," *Int. J. Quantum Chem.*, vol. 97, p. 651, 2004.

[138] T. Burnus, M. A. Marques, and E. K. Gross, "Time-dependent electron localization function," *Phys. Rev. A*, vol. 71, no. 1, p. 010501, 2005.

[139] J. Poater, D. M., M. Solà, and B. Silvi, "Theoretical evaluation of electron delocalization in aromatic molecules by means of atoms in molecules (AIM) and electron localization function (ELF) topological approaches," *Chem. Rev.*, vol. 105, no. 10, pp. 3911–3947, 2005.

[140] J. Sadhukhan, K. Mazurek, A. Baran, J. Dobaczewski, W. Nazarewicz, and J. Sheikh, "Spontaneous fission lifetimes from the minimization of self-consistent collective action," *Phys. Rev. C*, vol. 88, no. 6, p. 064314, 2013.

[141] J. Sadhukhan, J. Dobaczewski, W. Nazarewicz, J. Sheikh, and A. Baran, "Pairing-induced speedup of nuclear spontaneous fission," *Phys. Rev. C*, vol. 90, no. 6, p. 061304, 2014.

[142] J. Sadhukhan, K. Mazurek, J. Dobaczewski, W. Nazarewicz, J. Sheikh, and A. Baran, "Multidimensional skyrme–density–functional study of the spontaneous fission of $^{238}$U," *Acta. Phys. Pol. B*, vol. 46, no. 3, 2015.

[143] N. Schunck and L. Robledo, "Microscopic theory of nuclear fission: A review," *arXiv preprint arXiv:1511.07517*, 2015.

[144] J. McDonnell, W. Nazarewicz, J. Sheikh, A. Staszczak, and M. Warda, "Excitation-energy dependence of fission in the mercury region," *Phys. Rev. C*, vol. 90, no. 2, p. 021302, 2014.

[145] J. Dobaczewski, W. Nazarewicz, T. Werner, J. Berger, C. Chinn, and J. Dechargé, "Mean-field description of ground-state properties of drip-line nuclei: Pairing and continuum effects," *Phys. Rev. C*, vol. 53, no. 6, p. 2809, 1996.

[146] M. V. Stoitsov, J. Dobaczewski, W. Nazarewicz, S. Pittel, and D. J. Dean, "Systematic study of deformed nuclei at the drip lines and beyond," *Phys. Rev. C*, vol. 68, p. 054312, Nov 2003.

[147] I. Ragnarsson and S. Nilsson, *Shapes and Shells in Nuclear Structure*. Cambridge: Cambridge University Press, 2005.

[148] A. Bohr and B. R. Mottelson, *Nuclear Structure, vol. 2*. W. A. Benjamin, Reading, 1975.

[149] I. Ragnarsson, S. G. Nilsson, and R. K. Sheline, "Shell structure in nuclei," *Phys. Rep.*, vol. 45, no. 1, p. 1, 1978.

[150] W. Rae, "Clustering phenomena and shell effects in nuclear structure and reactions," *Int. J. Mod. Phys. A*, vol. 03, p. 1343, 1988.

[151] W. Nazarewicz, J. Dobaczewski, and P. V. Isacker, "Shell model calculations at superdeformed shapes," *AIP Conf. Proc.*, vol. 259, p. 30, 1992.

[152] P. A. Butler and W. Nazarewicz, "Intrinsic reflection asymmetry in atomic nuclei," *Rev. Mod. Phys.*, vol. 68, pp. 349–421, Apr 1996.

[153] H. Noto, Y. Abe, J. Hiura, and H. Tanaka, "An octupole deformation in $^{20}$Ne," *Prog. Theor. Phys.*, vol. 55, no. 5, pp. 1432–1447, 1976.

[154] T. Matsuse, M. Kamimura, and Y. Fukushima, "Study of the alpha-clustering structure of $^{20}$Ne based on the resonating group method for $^{16}$O+ $\alpha$ analysis of alpha-decay widths and the exchange kernel," *Prog. Theor. Phys.*, vol. 53, no. 3, pp. 706–724, 1975.

[155] L. Robledo and G. Bertsch, "Global systematics of octupole excitations in even–even nuclei," *Phys. Rev. C*, vol. 84, no. 5, p. 054302, 2011.

[156] A. Baran, A. Staszczak, J. Dobaczewski, and W. Nazarewicz, "Collective inertia and fission barriers within the skyrme–hartree–fock theory," *Int. J. Mod. Phys. E*, vol. 16, no. 02, pp. 443–451, 2007.

[157] A. Baran, K. Pomorski, A. Lukasiak, and A. Sobiczewski, "A dynamic analysis of spontaneous–fission half–lives," *Nucl. Phys. A*, vol. 361, no. 1, pp. 83–101, 1981.

[158] A. Baran, "Some dynamical aspects of the fission process," *Phys. Lett. B*, vol. 76, no. 1, pp. 8–10, 1978.

[159] A. Baran, Z. Łojewski, K. Sieja, and M. Kowal, "Global properties of even-even superheavy nuclei in macroscopic-microscopic models," *Phys. Rev. C*, vol. 72, no. 4, p. 044310, 2005.

[160] A. Baran, J. Sheikh, J. Dobaczewski, W. Nazarewicz, and A. Staszczak, "Quadrupole collective inertia in nuclear fission: Cranking approximation," *Phys. Rev. C*, vol. 84, no. 5, p. 054321, 2011.

[161] Y. Abe, S. Ayik, P.-G. Reinhard, and E. Suraud, "On stochastic approaches of nuclear dynamics," *Phys. Rep.*, vol. 275, no. 2, pp. 49–196, 1996.

[162] P. Fröbrich and I. Gontchar, "Langevin description of fusion, deep-inelastic collisions and heavy-ion-induced fission," *Phys. Rep.*, vol. 292, no. 3, pp. 131–237, 1998.

[163] N. Hinohara, "Collective inertia of the nambu-goldstone mode from linear response theory," *Phys. Rev. C*, vol. 92, no. 3, p. 034321, 2015.

[164] N. Hinohara and W. Nazarewicz, "Pairing nambu-goldstone modes within nuclear density functional theory," *Phys. Rev. Lett.*, vol. 116, no. 15, p. 152502, 2016.

[165] T. R. Rodríguez and G. Martínez-Pinedo, "Energy density functional study of nuclear matrix elements for neutrinoless $\beta$ $\beta$ decay," *Phys. Rev. Lett.*, vol. 105, no. 25, p. 252503, 2010.

[166] S. Dell'Oro, S. Marcocci, M. Viel, and F. Vissani, "Neutrinoless double beta decay: 2015 review," *Adv. High. Energy. Phys.*, vol. 2016, 2016.

[167] B. Schuetrumpf, M. A. Klatt, K. Iida, J. Maruhn, K. Mecke, and P.-G. Reinhard, "Time-dependent hartree-fock approach to nuclear "pasta" at finite temperature," *Phys. Rev. C*, vol. 87, no. 5, p. 055805, 2013.

[168] E. Engel and R. M. Dreizler, *Density functional theory: an advanced course*. Springer Science & Business Media, 2011.

[169] A. Becke, "Hartree–fock exchange energy of an inhomogeneous electron gas," *Int. J. Quantum Chem.*, vol. 23, no. 6, pp. 1915–1922, 1983.